ENSO and Pacific Decadal Variability in the Community Earth System Model Version 2

A. Capotondi[1,2], C. Deser[3], A. S. Phillips[3], Y. Okumura[4], and S. M. Larson[5]

[1]Cooperative Institute for Research in Environmental Sciences, University of Colorado, Boulder, CO

[2]Physical Sciences Division, NOAA/Earth System Research Laboratory, Boulder, CO

[3]Climate and Global Dynamics Division, NCAR, Boulder, CO

[4]Institute for Geophysics, University of Texas, Austin, TX

[5]Department of Marine, Earth, and Atmospheric Sciences, North Carolina State University, Raleigh, NC

Corresponding Author: Antonietta Capotondi (antonietta.capotondi@noaa.gov)

Key Points:

- El Niño Southern Oscillation in the model exhibits realistic timescale, precursors, temporal evolution, and teleconnections
- The El Niño Southern Oscillation amplitude is about 30% larger than observed, with anomalies displaced too far west than observed
- The model Pacific Decadal Variability has a realistic spatial pattern

Abstract

This study presents a description of the El Niño Southern Oscillation (ENSO) and Pacific Decadal Variability (PDV) in a multi-century preindustrial simulation of the Community Earth System Model version 2 (CESM2). The model simulates several aspects of ENSO relatively well, including dominant timescale, tropical and extra-tropical precursors, composite evolution of El Niño and La Niña events, and ENSO teleconnections. The realistic simulation of ENSO spectral characteristics is consistent with the spatial pattern of the anomalous equatorial zonal wind stress in the model, which results in the correct adjustment timescale of the equatorial thermocline according to the delayed/recharge oscillator paradigms. The realistic timescale of the equatorial thermocline adjustment is also reflected in the realistic time evolution of the equatorial Warm Water Volume. PDV in the model exhibits a pattern that is very similar to the observed, with realistic tropical and South Pacific signatures which were much weaker in some of the CESM2 predecessor models. The tropical component of PDV also shows a realistic association with ENSO decadal modulation. However, the ENSO amplitude is about 30% larger than observed in the preindustrial CESM2 simulation, and even larger in the historical ensemble, perhaps as a result of anthropogenic influences. In addition, the largest variability is found in the central Pacific rather than the eastern Pacific, as in observations, a discrepancy that somewhat hinders the model's ability to represent a full diversity in El Niño spatial patterns and appears to be associated with an unrealistic confinement of the precipitation anomalies to the western Pacific.

1. Introduction

The El Niño Southern Oscillation (ENSO) is the dominant mode of variability in the tropical Pacific at interannual timescales. This naturally occurring phenomenon is characterized by warm conditions in the central/eastern equatorial Pacific, known as El Niño events, which occur every two to seven years and alternate with the cold La Niña phase. A sea level pressure seesaw, known as the "Southern Oscillation", constitutes the atmospheric component of this coupled phenomenon (McPhaden et al., 2006). The tropical Pacific sea surface temperature (SST) anomalies associated with ENSO alter tropical convection and trigger atmospheric teleconnections which are responsible for worldwide temperature and precipitation impacts of critical societal importance (Ropelewski and Halpert 1987; Glantz, 2000, Tippett and Barnston, 2008).

The evolution of the equatorial Pacific upper-ocean heat content provides memory to the coupled equatorial system, and is primarily responsible for the quasi-cyclic nature of ENSO. However, stochastic atmospheric and oceanic variability within the tropical Pacific, as well as influences from the extra-tropical Pacific (Chiang and Vimont, 2004; Zhang et al., 2014) and from other ocean basins (Cai et al. 2019), which themselves may be stochastic in nature, result in deviations of the ENSO evolution from a regular cycle, and may contribute to event-to-event differences in spatial pattern, amplitude and temporal evolution. Slow variations of the tropical background conditions may also lead to a low-frequency modulation of ENSO characteristics (Fedorov and Philander, 2000; Capotondi and Sardeshmukh, 2017).

A large body of literature has recently emphasized the diversity in ENSO amplitudes and spatial patterns (Capotondi et al., 2015; Timmerman et al., 2018, Okumura et al., 2019, and references therein) which may result in different ENSO impacts both within the tropical Pacific (Dewitte et al., 2012; Turk et al., 2011; Radenac et al., 2012; Gierach et al., 2012; Lee et al., 2014) and remotely (Ashok et al., 2007; Larkin and Harrison, 2005, Patricola et al., 2019, among others). El Niño events with the largest anomalies in the far eastern Pacific produce intense rainfall in that usually cold and dry region. These events also greatly reduce equatorial upwelling in the eastern Pacific with dramatic consequences for ocean productivity and marine life. Warm ENSO events with largest anomalies located in the central equatorial Pacific, on the other hand, may be

associated with neutral and cooler conditions in the eastern Pacific, but lead to a reduction of marine productivity in the area where the largest anomalies occur (Gierach et al., 2012). The location of ENSO-related SST anomalies appears to also affect atmospheric teleconnections. Ensembles of atmospheric general circulation model simulations forced by small patches of SST anomalies prescribed at regularly spaced locations over the tropical Indo-Pacific domain showed that the area that is most effective in forcing the Pacific North American pattern (PNA) is the central-western Pacific, not the eastern Pacific where "canonical" El Niño events tend to have their largest signal (Barsugli and Sardeshmukh, 2002). Consistent with the results of Barsugli and Sardeshmukh (2002), anomalies in the central-western equatorial Pacific were identified as the most effective in forcing ocean warming along the U.S. West Coast (Shi et al., 2019; Capotondi et al., 2019), while precipitation in Southern California appeared to respond more strongly to SST anomalies in the eastern equatorial Pacific (Shi et al., 2019). The presence of a large level of atmospheric noise may, however, obscure the influence of ENSO diversity on atmospheric teleconnections and associated temperature and precipitation impacts over North America (Deser et al., 2018).

The complexity of ocean-atmosphere feedbacks underlying ENSO evolution and diverse expressions makes the simulation of ENSO by climate models extremely challenging. A steady progress in the representation of ENSO has been documented (Guilyardi et al., 2012; Bellanger et al., 2014) across the generations of models participating in the Climate Model Intercomparison Projects phases 3 and 5 (CMIP3 and CMIP5). For example, the large spread in ENSO amplitude exhibited by the CMIP3 models was largely reduced in the CMIP5 archive, and the ENSO seasonal phase locking was found modestly improved in the CMIP5 relatively to CMIP3 multi-model ensembles (Bellenger et al. 2014). Important improvements were detected in the National Center for Atmospheric Research Community Climate System Model version 4 (NCAR-CCSM4) relative to its predecessor CCSM3 (Deser et al., 2012). Unlike CCSM3, which exhibited a quasi-regular biennial ENSO behavior, CCSM4 had a broader spectral peak with a dominant timescale closer to the observed, an improvement that was attributed to a more realistic spatial pattern of the wind stress response to ENSO SST anomalies (Capotondi et al., 2006), and to a larger level of atmospheric noise (Neale et al., 2008). Unlike CCSM3, CCSM4 was also able to more realistically

simulate observed asymmetries in spatial pattern and duration between El Niño and La Niña events (Deser et al., 2012).

In spite of these improvements, notable biases in the representation of ENSO in climate models persist. One of these biases is the excessive westward extension of the SST anomalies associated with ENSO, a bias that could affect the models' ability to produce realistic teleconnections (Bellenger et al., 2014). A related issue is the models' difficulty to simulate the observed broad range of El Niño spatial patterns (Capotondi et al., 2015b; Capotondi et al., 2019). This problem appears to arise from the intensity of the eastern Pacific "Cold Tongue", which in the models tends to be larger than in nature (Ham and Kug, 2012). Since anomalous convective activity depends on the total SST relative to the tropical mean SST (He et al., 2018), an excessively cold mean eastern tropical Pacific will be unable to support local convection, even in the presence of positive SST anomalies, resulting in an atmospheric response confined to the western part of the basin, and a more limited range of SST anomaly patterns (Ham and Kug, 2012; Kug et al., 2012).

Apart from the interannual variations associated with ENSO in the tropical Pacific, the Pacific sector also exhibits variability at decadal and multidecadal timescales (Mantua et al. 1997; Zhang et al., 1997; Deser et al., 2004; Newman et al., 2016). The dominant pattern of variability in the North Pacific was identified as the leading empirical orthogonal function (EOF) of monthly SST anomalies poleward of 20°N, and termed the Pacific Decadal Oscillation (PDO) by Mantua et al. (1997). The PDO is characterized by anomalies of one sign in the central North Pacific, and anomalies of the opposite sign along the west coast of North America and the Gulf of Alaska. EOF analysis of low-pass filtered SST anomalies over the entire Pacific basin reveals a pattern that is quasi-symmetric about the equator, known as the Interdecadal Pacific Oscillation (IPO, Power et al., 1999), and "ENSO-like" in the tropical Pacific (Zhang et al., 1997). While both the PDO and IPO have been viewed as "modes" of variability, and related to important climatic and ecological impacts, recent research (Newman et al., 2016) has shown that the PDO should be seen, instead, as the result of a combination of different processes, including ENSO teleconnections, ocean mixed layer "re-emergence" mechanism (Alexander et al., 1999), and slow propagation of midlatitude Rossby waves (Kwon and Deser, 2007). In addition, although the PDO and IPO patterns are associated with variability at decadal-interdecadal timescales, no statistically

significant peak is usually found in the spectra of their associated time series, suggesting that these low-frequency variations may simply represent the low-frequency tail of a red-noise process, rather than a real oscillatory behavior. For this reason, we will refer to these decadal variations as "Pacific Decadal Variability" (PDV).

In this paper, we document ENSO and PDV in the latest version of the National Center for Atmospheric Research (NCAR) Community Earth System Model Version 2.1 (CESM2.1). Given the key role played by ENSO in the global climate system, the model's ability to realistically simulate ENSO is of paramount importance. We start by describing the model, the observational datasets used for its validation, and the Linear Inverse Modeling (LIM) approach employed for model diagnostics in section 2. In section 3, we examine ENSO in CESM2 relative to observations and to previous NCAR model versions. We will consider, in particular, ENSO temporal evolution and spectral characteristics, precursors, spatial diversity and teleconnections. PDV is briefly described in section 4, and conclusions are drawn in section 5.

2. Model descriptions, observational datasets, and LIMs

2.1 CESM2

CESM2 is the latest version of the NCAR suite of climate and earth system models. It includes fully interactive ocean, atmosphere, ice, land and ocean biogeochemical components, building on component models used in previous versions, but with important improvements in each of them. Specifically, the atmospheric component, the Community Atmospheric Model version 6 (CAM6) has improved parameterizations of all physical processes, the most notable of which is a new representation of convection through the unified turbulent scheme Cloud Layers Unified by Binormals (CLUBB, Golaz et al., 2002). The ocean component is based on the Parallel Ocean Program version 2 (POP2; Smith et al., 2010) with several physical and numerical improvements, including, among others, the use of prognostic chlorophyll for short-wave absorption, and the inclusion of a wave model and associated Langmuir mixing parameterization (Li et al., 2016). Additional details on all the component models can be found in Danabasoglu et al. (2019).

CESM2 has contributed simulations to the Climate Model Intercomparison Project phase 6 (CMIP6), including pre-industrial, historical, and future scenario simulations. For this study we will focus primarily on the pre-industrial control simulation (piControl) under 1850 radiative forcing conditions, supplemented as needed with a 11-member ensemble of historical simulations (HIST) and a 10-member ensemble of historical AMIP simulations with specified observed SSTs. All simulations are conducted at a nominal 1° horizontal resolution. The piControl is 1200 years long, but due to the presence of trends during the first 200 years, our analyses are restricted to model years 201-1200. Details of the spin-up and initialization procedures for the piControl and HIST ensemble are given in Danabasoglu et al. (2019).

For some of the diagnostics, we compare CESM2 with previous model versions, specifically Community Climate Model version 4 (CCSM4, Gent et al., 2011) and CESM version 1 (CESM1; Hurrell et al., 2013). Extensive documentation of ENSO and PDV in CCSM4 was provided in Deser et al. (2012). A dynamical analysis of ENSO in CESM1 is given in DiNezio et al. (2017a and b). For consistency with the length of the CESM2 piControl record analyzed, we used comparable durations for the pre-industrial control runs of CCSM4 (model years 301-1300) and CESM1 (model years 1201-2200).

2.2 Observational datasets

We use the following data sets for model validation.

1) SST from the NOAA Extended Reconstructed SST version 5 (ERSSTv5; Huang et al., 2017) over the period 1900-2018.

2) Sea level pressure (SLP) from the National Center for Environmental Prediction (NCEP) – NCAR Reanalysis (Kalnay et al., 1996), and from ERA20C (Poli et al., 2016) updated with ERA-Interim (Dee et al., 2011).

3) Precipitation from the NOAA reconstructed precipitation dataset (Chen et al., 2002) and from GPCP (Adler et al., 2003).

4) Surface winds from ERA5 (Hersbach et al., 2019) and surface wind stress from the NCEP-Department of Energy (DOE) atmospheric reanalysis (Kanamitsu et al., 2002).

5) Sea surface height (SSH) from the European Center for Medium-Range Weather Forecasting (ECMWF) Ocean Reanalysis System 4 (ORAS4; Balmaseda et al., 2013), covering the period 1958-2015.

6) Near-surface air temperature from Berkeley Earth Surface Temperature (Rohde et al., 2013).

2.3 Linear Inverse Model

To aid with model diagnostics we use a Linear Inverse Model (LIM). LIMs are empirical models that have been extensively used to understand and predict ENSO (Penland and Sardeshmukh, 1995). In the LIM framework, the tropical Pacific is described in terms of an anomaly state vector $\boldsymbol{x}$, which is constructed from anomalies of the key system variables. The evolution of $\boldsymbol{x}$ is then modeled in terms of linearly damped and stochastically perturbed dynamics (Penland and Sardeshmukh, 1995; Newman et al., 2011) of the form:

$$d\boldsymbol{x} = \boldsymbol{L}\,\boldsymbol{x}\,dt + \boldsymbol{S}\,\boldsymbol{r}\sqrt{dt} \qquad (1),$$

where the matrix $\boldsymbol{L}$ encapsulates the predictable dynamics of the system, the matrix $\boldsymbol{S}$ represents the spatially varying amplitude of the stochastic forcing, and $\mathbf{r}$ is a vector of random numbers drawn from a normal distribution with zero mean and unit standard deviation. The operators $\boldsymbol{L}$ and $\boldsymbol{S}$ can be estimated directly from the instantaneous and lagged covariance matrices of $\boldsymbol{x}$ (Penland and Sardeshmukh, 1995). The leading eigenvectors of the $\boldsymbol{L}$ operator, known as Empirical Normal Modes (ENMs), are non-orthogonal and damped, and may have an oscillatory component. In such a system, temporary growth is possible through a constructive superposition of the ENMs, which allow the identification of the optimal initial conditions conducive to the mature ENSO phase. In this study, we will use the LIM approach for two purposes: 1) Objectively determine the optimal ENSO precursors (the optimal initial LIM structures), and 2) Assess uncertainties of spectral estimates from multi-millennia synthetic time series of $\boldsymbol{x}$, determined through the integration of (1), which, by construction, are consistent with the statistics of the data used to train the LIM (Capotondi and Sardeshmukh, 2017). We construct LIMs for both observations and CESM2, using SST and SSH as state variables. The observational LIM is trained on SST from ERSSTv5 and SSH from ORAS4 over the period 1958-2014, while the CESM2 LIM is based on model years 201-

1200. To reduce the number of degrees of freedom, the SST and SSH anomalies are projected onto their leading Empirical Orthogonal Functions (EOFs). We retain 20 SST and 10 SSH EOFs for both observations and CESM2, accounting for 94% (72%) of the SST (SSH) variance in observations, and 86% (77%) of the variance in CESM2.

3. ENSO

3.1 Nino-3.4 SST variability

ENSO characteristics, such as amplitude and dominant timescale, are strongly dependent on the equatorial Pacific mean state (Fedorov and Philander, 2000). In particular, the mean zonal SST gradient, which is strongly affected by the strength of the eastern Pacific "Cold Tongue", was identified by Fedorov and Philander (2000) as a key parameter for ENSO stability characteristics. The mean climatological SST conditions in CESM2 are compared with ERSSTv5, CESM1 and CCSM4 in Fig. 1. The intensity and zonal extent of the equatorial Cold Tongue, as indicated by the westward penetration of the 27°C isotherm (thick white contour), appear to be improved in CESM2 compared to CCSM4, and especially to CESM1, relative to the ERSSTv5 dataset.

The standard deviation of monthly SST anomalies, where anomalies are defined as the departures from the long-term monthly means, in the central/eastern tropical Pacific are overestimated by about 30%-40% in all three models relative to ERSSTv5. Apart from the amplitude, the spatial pattern of the variability also shows discrepancies with the observed. While ERSSTv5 exhibits the largest standard deviations in the far eastern Pacific, the largest standard deviations are achieved around 110°W in CCSM4, near 120°W and 180° in CESM1, and near 180° in CESM2. SST variability is also overestimated by the models in the Kuroshio Extension region and in the Bering Sea. CESM1 and CESM2 slightly underestimate the observed variability in the Gulf of Alaska and along the northern part of the US West Coast.

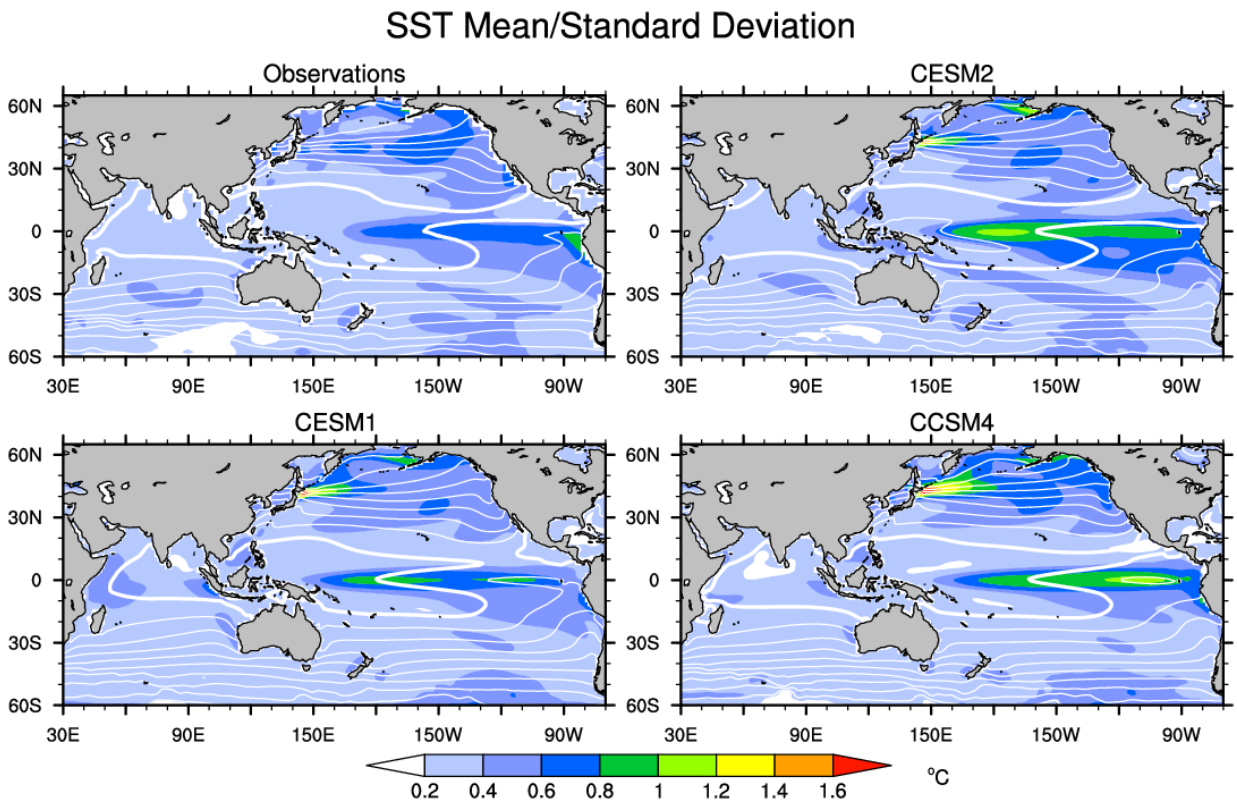

Figure 1. Mean SST (white contours) and SST monthly standard deviation (color shading) for detrended ERSSTv5 over 1900-2018 (top-left), and 1000-year segments of the pre-industrial control simulations of CESM2 (top right), CESM1 (bottom-left), and CCSM4 (bottom-right). Contour interval is 3°C and the thick white contour indicates the 27°C isotherm.

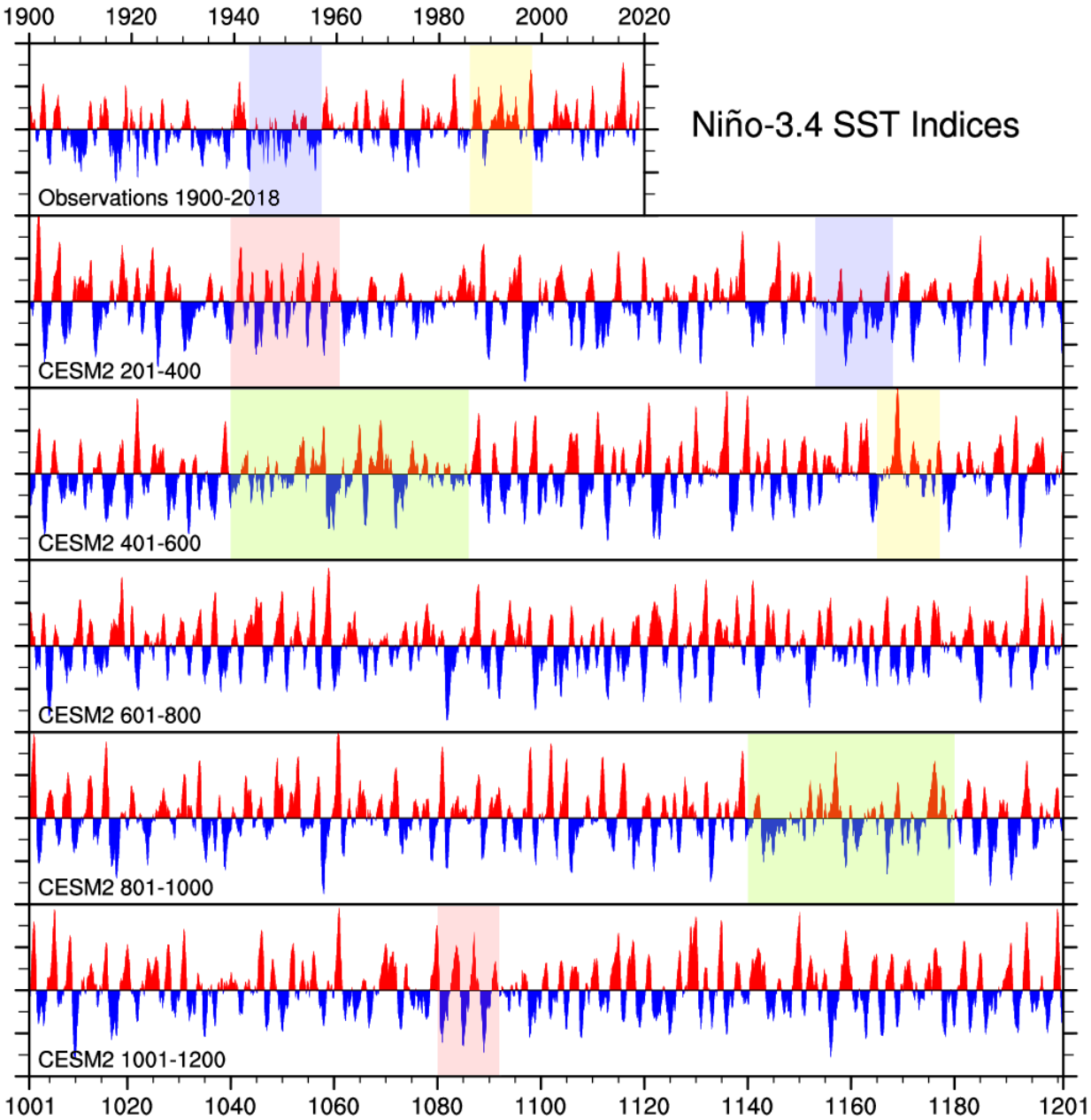

Figure 2. Time series of the monthly Niño-3.4 index for ERSSTv5 over the 1900-2018 period (top panel) and for CESM2, from model year 201 to 1200 (rows 2-6), with each row displaying a 200-yr segment of the Niño-3.4 index. Vertical axis ranges from -4°C to 4°C in all panels. Shading is used to highlight periods with different characteristics of the Niño-3.4 index as described in the text.

The Niño-3.4 index, defined as the area average of monthly SST anomalies in the region 5°S-5°N, 170°-120°W, is a commonly used index to represent SST variability associated with ENSO (e.g., Trenberth et al., 2002). The evolution of the Niño-3.4 index over the piControl simulation of CESM2 is compared in Fig. 2 with the evolution of the Niño-3.4 index from ERSSTv5 over the

1900-2018 period. Although the amplitude of the Niño-3.4 index in the model is overall larger than in ERSSTv5 (the Niño-3.4 standard deviations are 0.87 for ERSSTv5 and 1.14 for CESM2 over the periods shown in Fig. 2), with some extreme events as large as 4°C in the model, its temporal evolution shows similar visual behavior to the observed in terms of dominant timescale and degree of irregularity. For example, prevailing La Niña conditions, similar to those observed during 1942-1957, are also seen in CESM2 (e.g., during model years 352-368, light blue shading), and periods dominated by warm events such as 1982-1998 in observations are also seen in CESM2 (e.g., model years 565-578, yellow shading). The millennial-long model time series also highlights the presence of low-frequency modulation of ENSO characteristics, with decadal periods characterized by a more regular, quasi-oscillatory ENSO behavior (e.g., during model years 240-260, and 1080-1092, pink shading) relative to other periods with a more irregular alternation of warm and cold events (e.g., years 440-485 and 940-980, green shading). These decadal variations in the Niño-3.4 characteristics, which were already noted by Wittenberg (2009) for the GFDL_CM2.1 model and Deser et al. (2012) for CCSM4, open the question of how robustly we can characterize ENSO from the relatively short instrumental records.

Observed ENSO events peak in boreal winter, with a minimum in late spring, as illustrated by the monthly standard deviations of the ERSSTv5 Niño-3.4 index in Fig. 3 (top-left). This seasonal phase locking has been a difficult aspect for climate models to simulate correctly (Bellenger et al., 2014), with models often exhibiting a secondary peak in a different part of the year, or showing comparable standard deviations in boreal winter and spring-summer. CCSM4, CESM1, and CESM2 all achieve their largest variance in December and January, and a minimum in late spring-summer, consistent with ERSSTv5 (although the minimum in CESM1 and CESM2 is delayed by 1-2 months compared to observations; Fig. 3, left panels). The monthly standard deviations also highlight the larger ENSO amplitude in the models (especially CESM2) than the observations in all months.

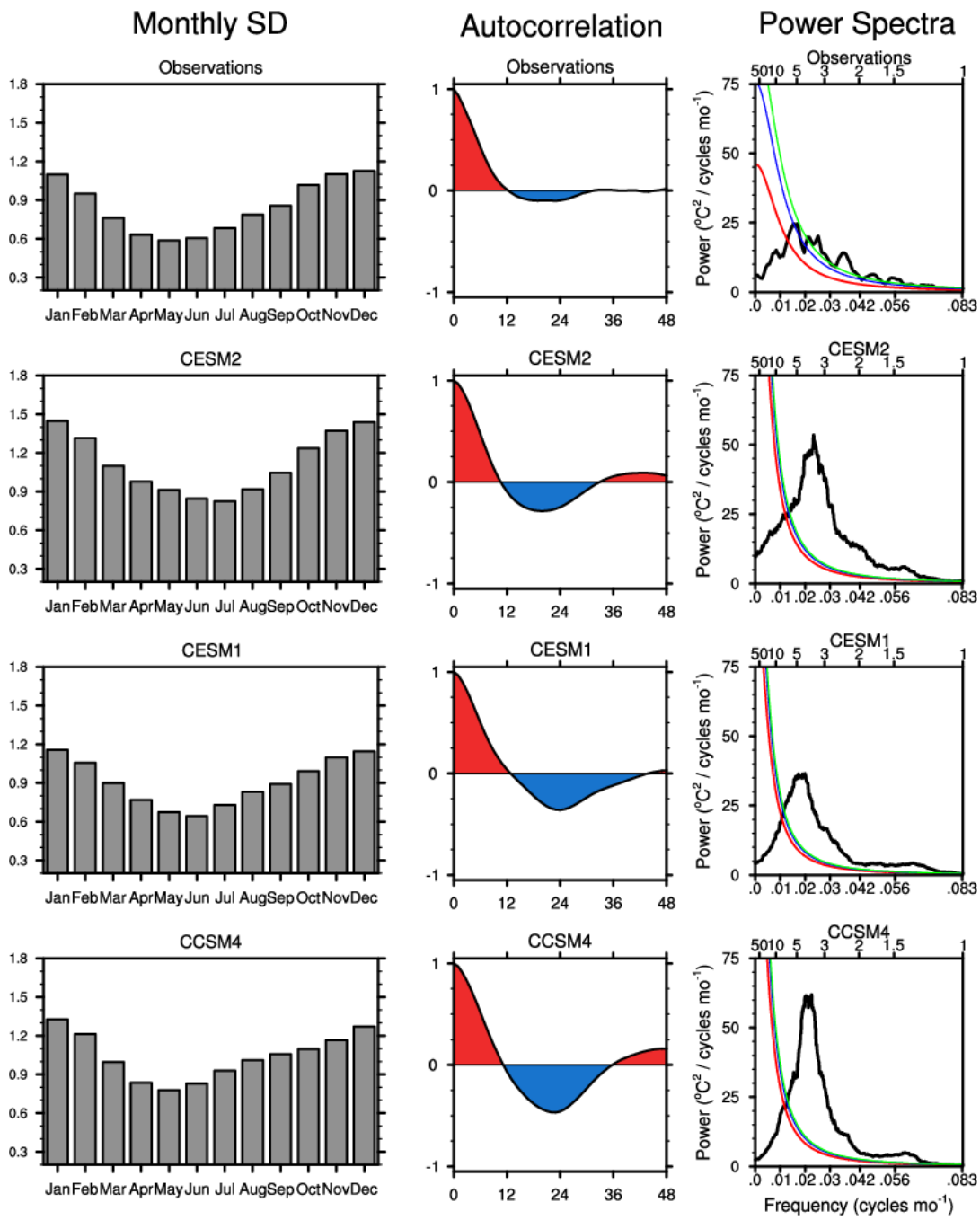

Figure 3. Monthly standard deviations (left panels), auto-correlation functions (middle panels) and power spectra (right panels) of the Niño-3.4 index for observations (detrended ERSSTv5 during 1900-2018, top row), CESM2 (model years 201-1200, second row), CESM1 (model years 1201-2200, third row) and CCSM4 (model years 301-1300, bottom row). The x-axis in the autocorrelation function indicates the lag in months. The red, blue and green curves in the right panels indicate the Markov red-noise spectrum, and its 95% and 99% confidence bounds, respectively. Top axis in the right panels indicates period in years.

The power spectrum of the Niño-3.4 index from ERSSTv5 shows a broad maximum with timescales ranging from approximately 2.5 to 8 years (Fig. 3, top right). The spectra of CESM2, CESM1 and CCSM4 are dominated by a pronounced spectral peak which is well within the 2.5-8 years observational range (Fig. 3, right panels). As noted before, ENSO is stronger in the models than in observations, especially in CCSM4 and CESM2. Another way to characterize the ENSO temporal evolution is through the lag autocorrelation function of the Niño-3.4 index (Fig. 3, middle panels). In all cases, the zero-crossing occurs at a lag of 11-12 months. The maximum negative correlation occurs at a lag of 18-24 months for ERSSTv5, 23-24 months in CESM1 and CCSM4, and 18-21 months in CESM2. The magnitude of the maximum negative correlation is larger in the models relative to observations, perhaps an indication of a more consistent and larger amplitude transition to the opposite phase of the ENSO cycle in the models than in ERSSTv5. However, given the difference in the duration of the Niño-3.4 index in the models than in the observations, it is unclear whether our relatively short observational sample is representative of the full range of ENSO statistics in the real world.

For a more direct comparison of CESM2 and ERSSTv5 we repeat the calculation of the monthly standard deviations, autocorrelation functions and spectra over the historical period 1958-2014 (Fig. 4). We establish the statistical significance of the CESM2 historical estimates by using all 11 CESM2 historical simulations, while for the observations we use a "synthetic observational ensemble" obtained from a multi-millennia LIM integration trained over the 1958-2014 period. The LIM is run for 28,500 years yielding 500 57-year segments that are used to estimate the observational uncertainty. The resulting ensemble spread, a measure of the internal system noise, is shown by the light blue shading in the middle and right panels of Fig. 4. For the monthly standard deviations (Fig. 4, left panels) boxplots are used to define minimum and maximum values, as well as the first, second (median) and third quartile of the probability density function of the standard deviations. The ENSO amplitude in the CESM2 historical ensemble is larger than in the piControl (note that the vertical axes in Figs. 4 are different than in Fig. 3), perhaps reflecting the influence of anthropogenic forcing on ENSO. As in piControl, the monthly standard deviations achieve their largest values in December and January, with a summer minimum that is delayed by about 2 months in CESM2 relative to observations. The availability of several ensemble members allows the detection of a negative skewness in the CESM monthly standard deviations. This asymmetry

is not present in the distributions of monthly standard deviations obtained from the LIM, likely due to the assumption of a Gaussian noise distribution of the LIM methodology. The ensemble mean autocorrelation function of CESM2 over 1958-2014 is in very good agreement with the observed, with the first zero-crossing at a lag of about 12 months, the negative minimum at a lag of 18-24 months, and the second zero crossing at a lag of about 30 months. As for piControl, the CESM2 spectrum in the historical period displays a peak between 2.8-8 years in agreement with the observed, but with an approximately 40% larger amplitude. This amplitude discrepancy is put in a broader perspective by the large range of spectral estimates that can arise purely from sampling variability, as assessed through the use of an ensemble of simulations that differ only by small changes in initial conditions. This large level of uncertainty highlights how the availability of only one observational realization may hinder our ability to meaningfully compare models and observations.

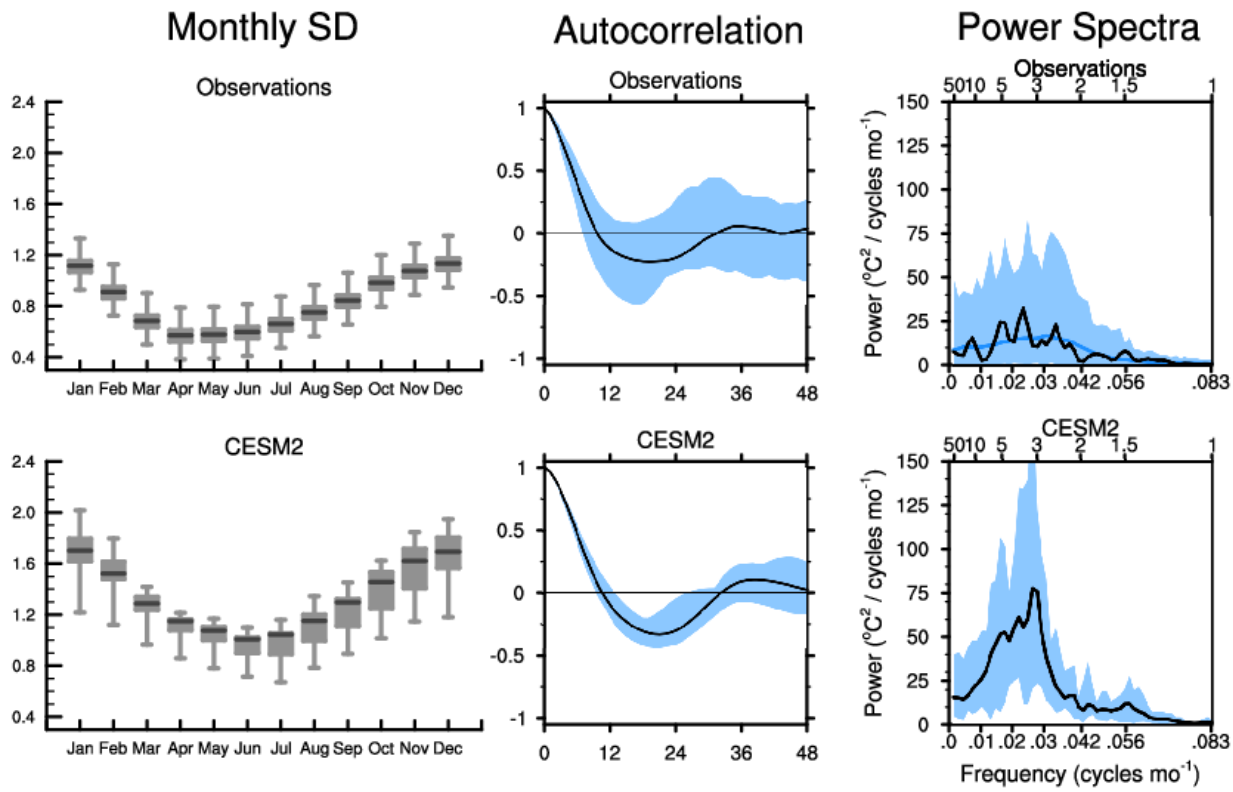

Figure 4. Monthly standard deviation (left panels), autocorrelation function (middle panels) and power spectra (right panels) of the detrended Niño-3.4 index during 1958-2014 for observations (ERSSTv5, top panels) and CESM2 historical simulations (bottom panels). The range of estimates for the CESM2 autocorrelation function and spectrum (light blue shading) are estimated using the 11-member ensemble of the CESM2 historical simulations, while the observational uncertainties are based on a 28,500 year LIM integration, yielding 500 57-year segments that are consistent with

the statistics of the 1958-2014 period used to train the LIM. The statistics of the monthly standard deviations in the left panels are summarized through the use of boxplots showing the minimum values (whiskers minima), first quartiles (lower edge of the boxes), median (black lines), third quartiles (upper edge of the boxes) and maximum values (whiskers maxima) of the standard deviations for each month. The blue curve in the top-right panel shows the average spectrum of the 500 57-year segments of the LIM output. Note the different vertical axes between Figs. 3 and 4.

Previous studies (Kirtman et al., 1997; An and Wang, 2000; Capotondi et al., 2006) have related the dominant ENSO timescale to the spatial structure of the zonal wind stress response to the ENSO SST anomalies. Wind stress anomalies that are located further to the east, and have a broader meridional scale L_y are associated with longer ENSO timescales. These zonal wind stress anomalies are associated with Ekman pumping anomalies that can excite off-equatorial Rossby waves further away from the western boundary and from the equator. The decrease of the Rossby wave phase speed with latitude and the longer propagation distance from the generation longitude to the western ocean boundary lead to a longer adjustment timescale of the equatorial thermocline, and a longer ENSO timescale. The spatial patterns of the zonal wind stress associated with ENSO in observations and CESM2 are compared in Fig. 5. The patterns are obtained by regressing the zonal wind stress at each grid point on the normalized Niño-3.4 index. The zonal wind stress from the NCEP/DOE reanalysis, available over the period 1979-2018 is used as the observational estimate. The spatial pattern of the zonal wind stress in CESM2 has a somewhat excessive longitudinal elongation near the equator with a sharp transition to anomalies of the opposite sign along 4°N, from about 150°E to 120°W. However, it is centered at a similar longitude as observations (174°E vs. 177°E), and its meridional width L_y is very comparable with the observed (20° vs. 19° degrees of latitude), consistent with the realistic dominant timescale of the Niño-3.4 index in CESM2 relative to observations. A similar analysis reported by Deser et al. (2012) for CCSM4 and CCSM3 indicated a large improvement of the spatial pattern of the zonal wind stress in CCSM4 relative to CCSM3, which was viewed as an important contributing factor to the more realistic spectral characteristics of ENSO in CCSM4 relative to its predecessor CCSM3. These improved characteristics are retained in CESM2 (and CESM1). Our linear analysis of the wind stress response to the Niño-3.4 variations does not capture the asymmetry of the wind stress anomalies during warm and cold events, with anomalies being larger during El Niño events than

during La Niña events (Capotondi et al., 2018, and references therein). This ENSO feedback will be examined in detail in a future study.

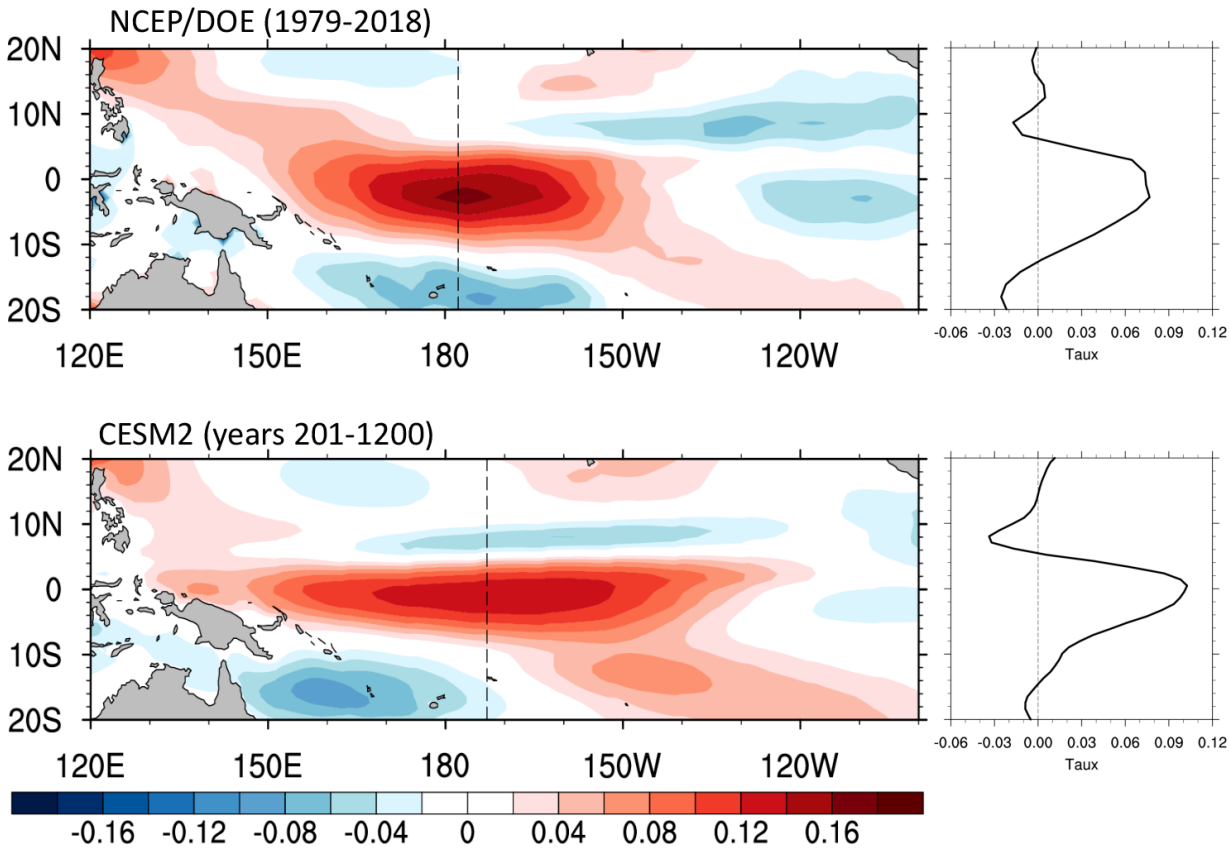

Figure 5. Regression of zonal wind stress upon the normalized Nino-3.4 index for observations (zonal wind stress from the NCEP/DOE reanalysis over 1979-2018, and Niño-3.4 index from detrended ERSSTv5 over the same time period, top-left) and CESM2 (years 201-1200, bottom-left) as a function of longitude and latitude, and their zonal average (right panels). Dashed line in the left panels shows the "center of mass" of the positive zonal wind stress anomalies computed as the equatorial (2°S-2°N) zonal wind stress anomaly weighted longitude between 140°E and 120°W. Right panels show the zonal average of the zonal wind stress, from 20°S to 20°N. The latitudes of zero crossing in the right panels are used to define the meridional scale L_y of the anomalous zonal wind stress for both observations and model. L_y is 18.8° of latitude for the observations and 20° for CESM2.

3.2 Composite evolution of El Niño and La Niña events

To compare the spatiotemporal evolution of El Niño and La Niña events between the models and observations, we conduct composite analysis following the methodology of Okumura and Deser (2010). For each model and observational SST dataset, El Niño (La Niña) events are selected when the December Niño-3.4 index exceeds 1 (is less than -1) standard deviation. Before selecting the

events, the monthly Niño-3.4 index is smoothed with a 3-month binomial filter to suppress subseasonal variability. When the El Niño or La Niña criterion is satisfied for consecutive years, it is counted as a single event. For each event, the year containing the December when the Niño-3.4 index first meets the criterion is denoted as year 0 and the subsequent years as year +1, year +2, …. Following this methodology, El Niño (La Niña) composites contain 20 (15) events for observations between 1900 and 2018, 142 (153) events for the CESM2 piControl, 130 (119) events for the CESM1 piControl, and 146 (139) events for the CCSM4 piControl.

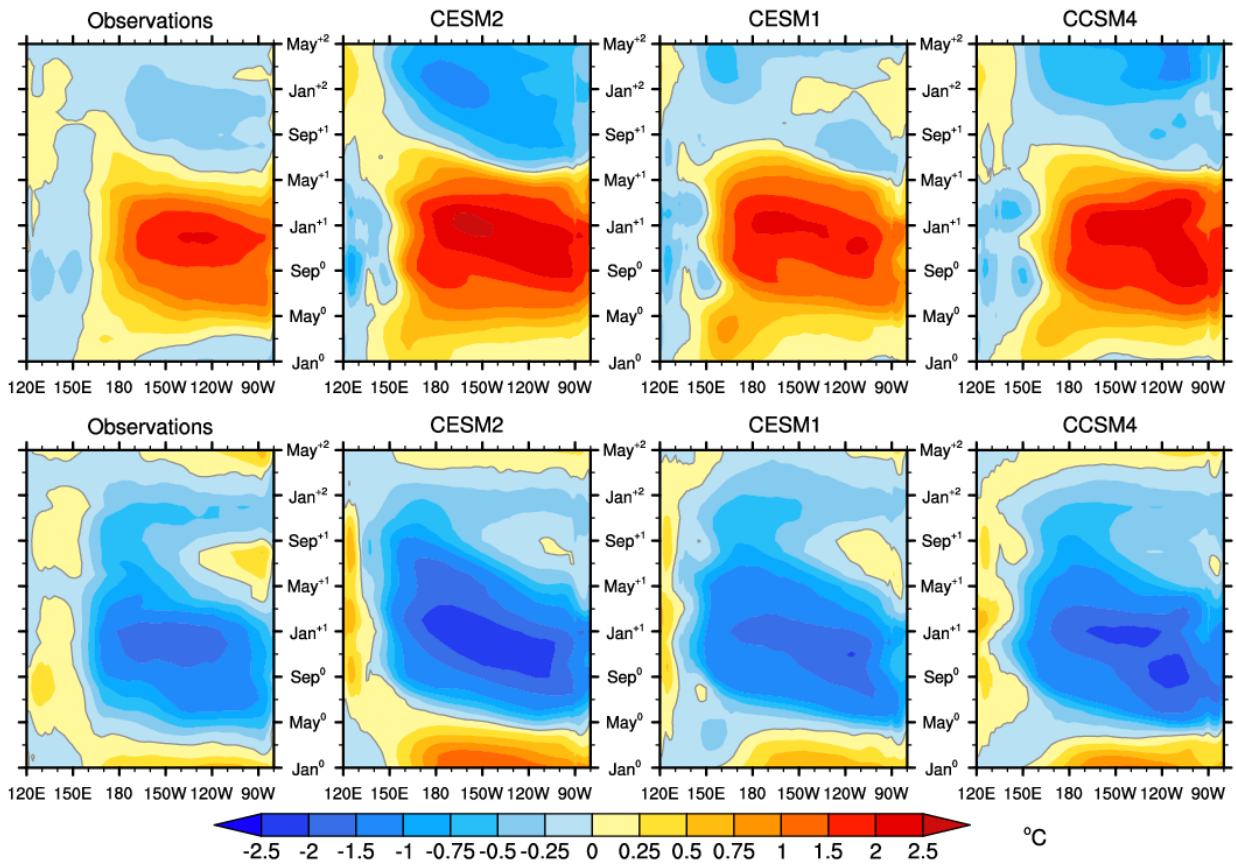

Figure 6. Longitude-time sections of composite SST anomalies along the equator (3°S-3°N) for (top) El Niño and (bottom) La Niña based on observations (ERSSTv5 over 1900-2018, left panels), CESM2 (model years 201-1200, second column), CESM1 (model years 1201-2200, third column), and CCSM4 (model years 301-1300, right panels). See text for details of the compositing methodology.

Longitude-time sections of SST anomalies along the equator for composite El Niño and La Niña events are presented in Fig. 6. CESM2 reproduces observed asymmetry in the duration of El Niño and La Niña events (e.g., Dommenget et al., 2013; Larkin & Harrison, 2002; McPhaden & Zhang, 2009; Ohba & Ueda, 2009; Okumura & Deser 2010), similar to CCSM4 (Deser et al., 2012) and

CESM1 (DiNezio et al., 2017; Wu et al., 2019). In both models and observations, composite El Niño terminates and transitions to a weak La Niña state in year +1, whereas composite La Niña persists and re-intensifies toward the end of year +1. Compared to the earlier versions of the model, CESM2 shows a stronger tendency for El Niño to transition to La Niña and a weaker tendency for La Niña to persist into year +1. Previous studies suggest that nonlinearities in both atmospheric and oceanic processes contribute to the asymmetric duration of El Niño and La Niña [see recent reviews by Okumura (2019) and An et al. (2019)]. Besides the event duration, all versions of the model simulate a zonal displacement of equatorial SST anomalies between El Niño and La Niña during year 0, with La Niña cooling shifted to the west by 10°-20° of longitude relative to El Niño. These equatorial SST anomalies during year 0 exhibit westward propagation. The re-intensification of La Niña near the end of year +1, on the other hand, occurs simultaneously across the basin in both models and observations.

Composite El Niño and La Niña events last one and two years, respectively, but individual events show diverse temporal evolution (Fig. 7). As in Deser et al. (2012), we define the duration of an El Niño (La Niña) event as the number of months for which the Niño-3.4 index remains above 0.25 standard deviations (below -0.25 standard deviations) of the monthly index after December of year 0. Frequency distributions of the event durations compare well between CESM2 and observations. In CESM2 (observations), 83% (80%) of El Niño events terminate in year +1, whereas 44% (50%) of La Niña events persist through year +1. The larger fraction of multi-year events for La Niña than El Niño is consistent with the overall asymmetry in their duration. Recent studies suggest that the duration of individual El Niño and La Niña events is controlled by multiple factors, including the magnitude of initial equatorial oceanic heat content anomalies, onset timing, and remote influences from the extratropical Pacific and the tropical Indian and Atlantic Oceans (DiNezio et al., 2017; Wu et al., 2019). It is noted that the fraction of multi-year events decreases for both El Niño and La Niña in CESM2 compared to CESM1 and CCSM4 (not shown), consistent with the differences shown in Fig. 6.

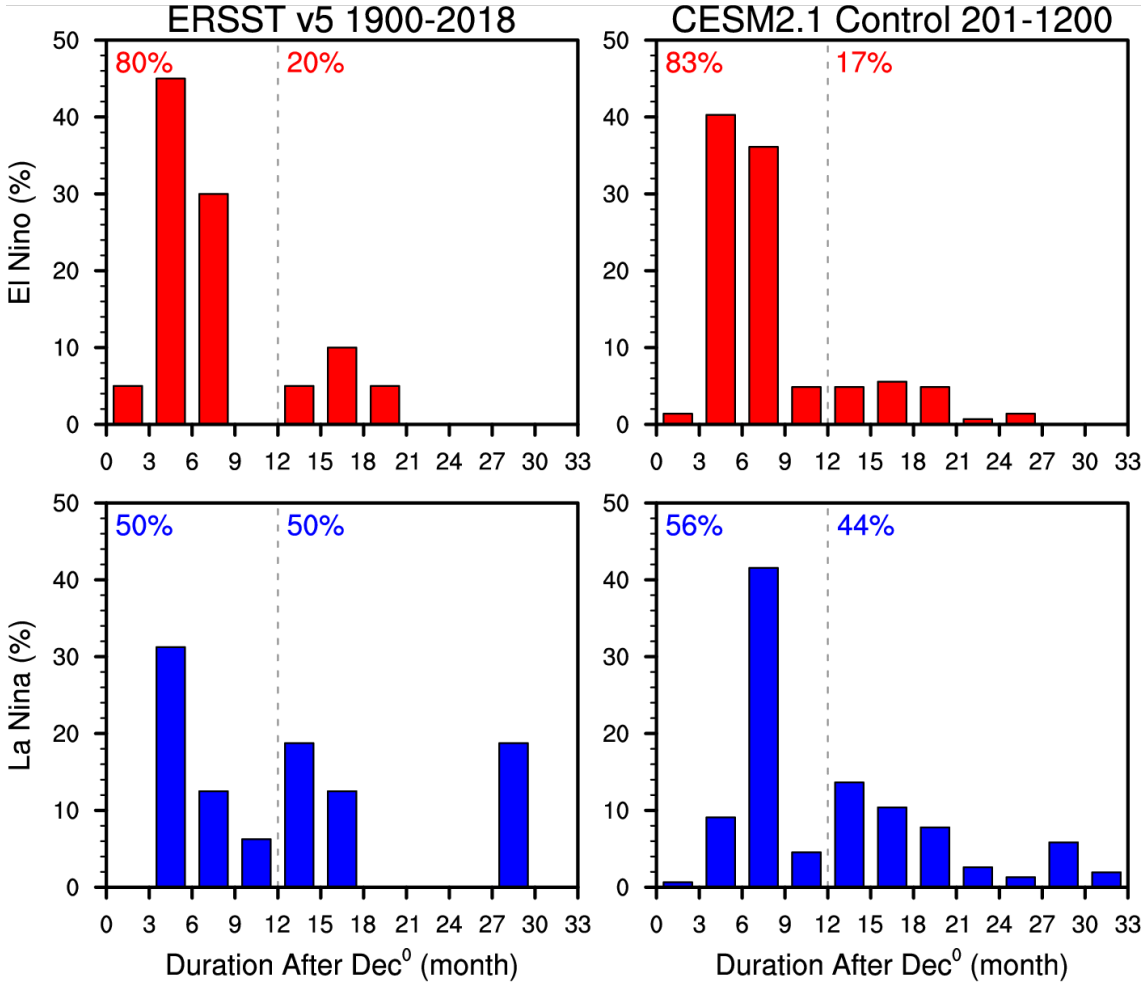

Figure 7. Frequency distribution (%) of (top) El Niño and (bottom) La Niña duration (in months) for (left) observations (detrended ERSSTv5 1900-2018) and (right) CESM2 control simulation (model years 201-1200). The El Niño (La Niña) duration is defined as the number of months for which the Niño-3.4 index remains above 0.25 standard deviations (below -0.25 standard deviations) after December of year 0. The number of El Niño (La Niña) events in each 3-month bin is divided by the total number of El Niño (La Niña) events. The numbers near the top of each panel indicate the fraction of events that terminate in year +1 (left numeral) and persist through year +1 (right numeral).

3.3 ENSO Precursors

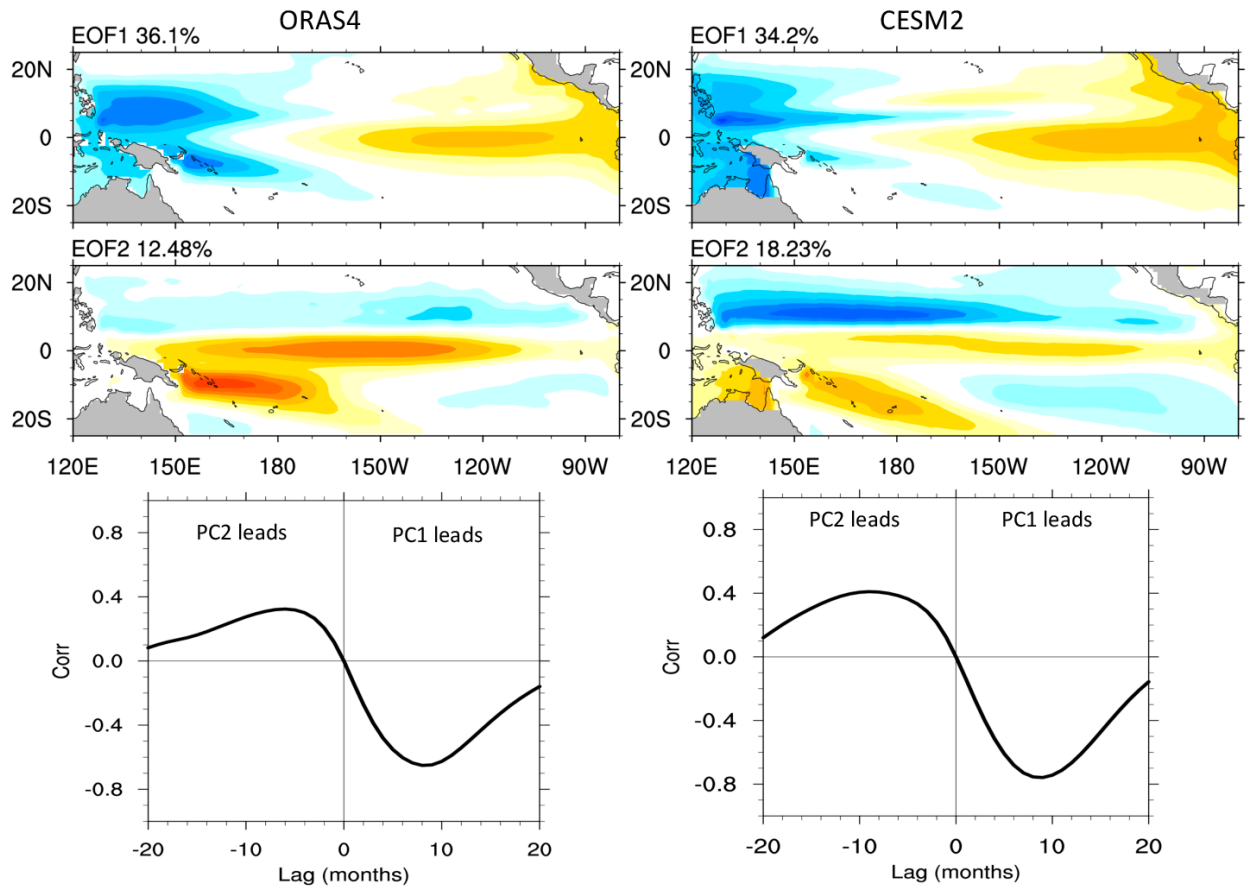

Figure 8. Leading EOFs of SSH for ORAS4 (1958-2014, left panels) and CESM2 (201-1200, right panels). Top panels show EOF1 for the two datasets, middle panels show EOF2, and bottom panels display the lag-correlation between the associated PCs, with PC1 leading PC2 for positive lags. In both ORAS4 and CESM2, the lag-correlations indicate that EOF1, associated with the peak of the positive ENSO phase, leads the negative phase of EOF2, i.e. a discharged equatorial Pacific thermocline. Conversely, a recharged state (positive EOF2) leads to the positive phase of EOF1, i.e., the development of an El Niño event.

Variations in equatorial upper-ocean warm water volume (WWV), usually described in terms of thermocline depth or sea surface height (SSH), are a fundamental component of ENSO evolution, as theoretically described by the recharge oscillator paradigm (Jin, 1997), and documented in observations (Meinen and McPhaden, 2000). The two leading EOFs of SSH effectively capture such variations as shown in Fig. 8 for both observations and CESM2. In both datasets, the leading SSH EOF exhibits a dipole pattern with positive anomalies (deeper thermocline) in the eastern equatorial Pacific, and negative anomalies (shallower thermocline) in the western Pacific. The

reduced zonal thermocline slope leads to an anomalous poleward flow, which discharges the WWV and leads to a shallower thermocline across the equatorial Pacific, as described by EOF2 (with the opposite sign). Upwelling of colder water in the eastern Pacific can then lead to the opposite La Niña phase. The dynamical relationship between EOF1 and EOF2 is encapsulated by the lead-lag relationship of the associated Principal Components (PCs, bottom panels of Fig. 8) showing that a recharged state (positive EOF2) tends to lead to a warm ENSO phase approximately a quarter of a cycle later, while positive EOF1 leads to the discharged state described by EOF2 with the opposite sign. The magnitude and lags of the maximum correlations are very similar in the model and observations, confirming the realistic time evolution of WWV in the model.

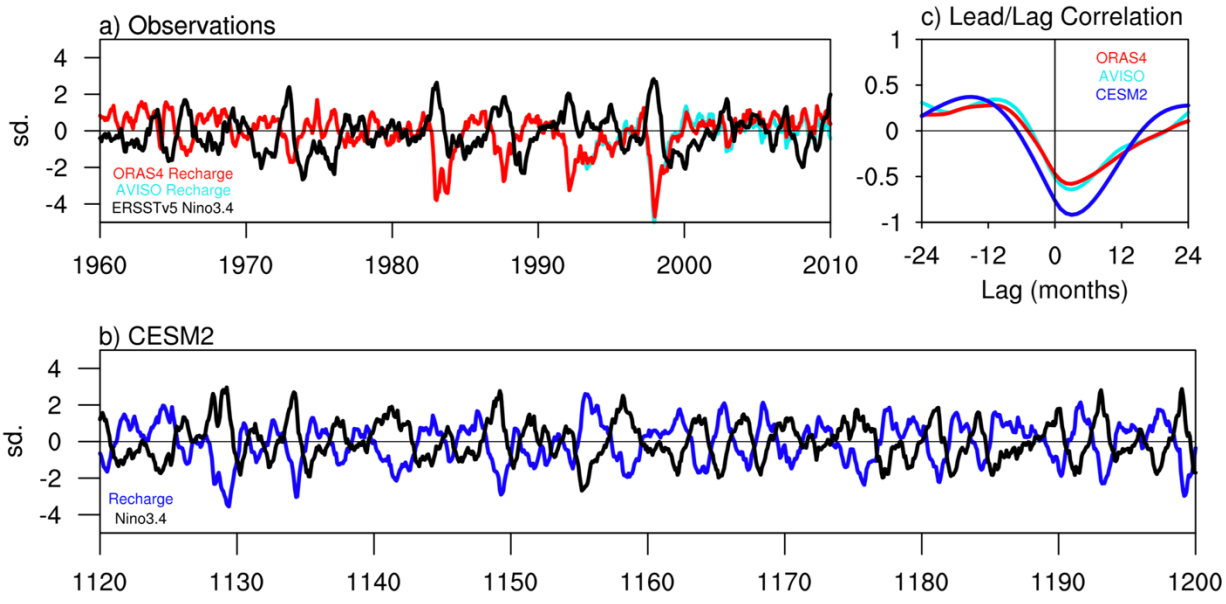

Figure 9. a) Time evolution of the observed recharge-discharge and Nino3.4 SST index over 1960-2010. The AVISO and ORAS4 estimates for the recharge are defined as the area-averaged sea surface height anomalies over 5°S-5°N, 120°E-155°W. AVISO coverage begins in 1993. b) As in a) but for CESM2 over years 1120-1200. The recharge is defined as the warm water volume integrated over 5°S-5°N, 120°E-155°W. All time series are standardized. c) Lead-lag correlations of Niño-3.4 and the recharge-discharge in observations and CESM2 (model years 800-1200). Positive (negative) lags indicates Niño3.4 leads (lags) the recharge.

While several studies have considered the WWV integrated across the entire equatorial Pacific, recent research has emphasized the key role of the western-to-central equatorial Pacific as a more effective ENSO predictor at lead times of about 1 year or longer (McGregor et al., 2016; Neske and McGregor, 2018; Izumo et al., 2019). The relationship between the WWV in the western-central Pacific (the "recharge") and the Niño-3.4 index is illustrated in Fig. 9 for several observational datasets and a subset of the CESM2 output. The positive correlation at negative lags

(recharge leading Niño-3.4) indicates that like-sign recharge-discharge precedes like-sign Niño-3.4. In other words, a recharge tends to occur prior to an El Niño and a discharge tends to occur prior to a La Niña. The negative correlation at positive lags (Niño-3.4 leading recharge) indicates that a net discharge of heat content occurs at and following the peak of an El Niño and a net recharge of heat content occurs at and following the peak of a La Niña, hence the correlation is negative. An asymmetry is found in the relative amplitude of the discharge versus the recharge in both observations and CESM2 (Fig. 10). Whether this amplitude asymmetry in the recharge-discharge translates into an asymmetry in ENSO predictability is still debatable (Planton et al., 2018, Larson and Kirtman, 2019, Larson & Pegion, 2019). That said, on average, in CESM2, La Niña events tend to follow a discharged state, whereas El Niño events appear to follow a neutral state.

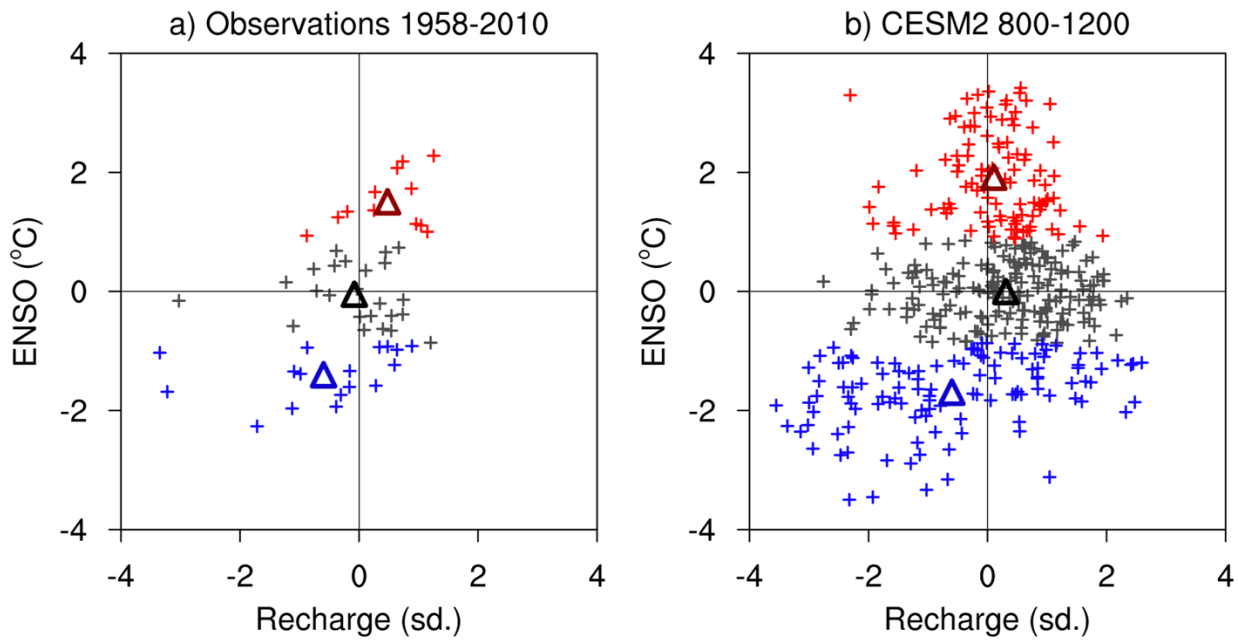

Figure 10. Scatterplot of the standardized March recharge-discharge with the following December Niño-3.4 SST anomaly in (left panel) observations and (right panel) CESM2 years 800-1200. Blue markers indicate La Niña events, black markers indicate neutral, and red markers indicate El Niño events. The threshold for El Niño (La Niña) is exceedance of the + (–) one standard deviation of the observed Niño-3.4 SST anomaly over 1958-2010. Bold triangles indicate the average over each of the 3 ENSO categories.

Apart from equatorial processes, the onset of ENSO events can also be affected by extra-tropical influences, including, for example, the Seasonal Footprinting Mechanism (SFM, Vimont et al., 2001) and the North and South Pacific Meridional Modes (NPMM and SPMM; Chiang and

Vimont, 2004; Zhang et al., 2014). The NPMM and SPMM are meridional dipole patterns of SST anomalies that result from changes in evaporative cooling associated with changes in the strength of the subtropical trade winds. They can influence equatorial processes through either the propagation of the SST anomalies to the equator (Chiang and Vimont, 2004; Larson et al., 2018) or through the dynamical adjustment of the equatorial thermocline induced by their associated wind anomalies (Alexander et al., 2010; Anderson et al., 2013). These extra-equatorial precursors are captured by the optimal initial conditions obtained with the LIM approach, as, by definition, these initial conditions provide the most effective forcing of the mature ENSO state (termed the "optimal final"). The optimal initial structure for the observational LIM (Fig. 11a), computed for a lead time of 8 months, displays positive SST anomalies extending from the coast of California to the equator, consistent with the NPMM (Chiang and Vimont, 2004), and positive anomalies extending to the equator along the southeastern Pacific coast, which are similar to the SPMM (Zhang et al. 2014). Positive SSH anomalies are present along the equator, indicative of a recharged state, while negative SSH anomalies in the northern tropics are indicative of westward propagating upwelling Rossby waves. This initial optimal structure evolves, eight months later, into a final optimal structure (Fig. 11c) that displays a "canonical" El Niño event, with the largest SST anomalies in the Niño-3.4 region, and SSH anomalies exhibiting the zonal dipole pattern associated with a reduced zonal slope of the thermocline. The optimal initial and final structures for CESM2 (Figs. 11b, d) show patterns qualitatively similar to the observed, with two notable differences: 1) A much larger SSH signal along the equator, likely indicative of a more pronounced role of recharge-discharge processes in the model, and 2) The equatorial signature of the NPMM displaced 15°-20° further west than in the observations, consistent with the westward displacement of the ENSO SST anomalies discussed in Fig. 1.

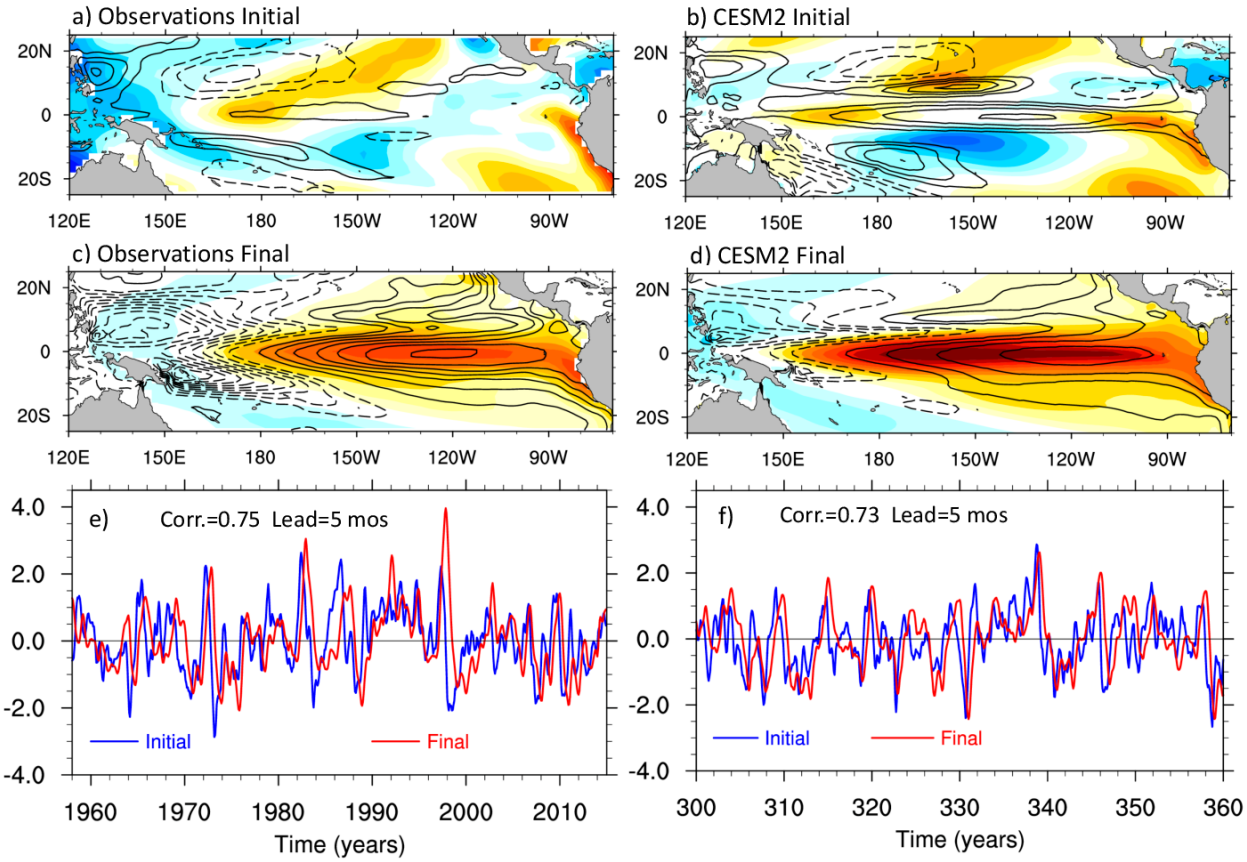

Figure 11. Initial (top panels) and final (middle panels) optimal structures obtained with LIMs trained on observations (left panels) and CESM2 (right panels). Shading is for SST and contours are for SSH. Bottom panels show the time series associated with the initial (blue) and final (red) optimal structures for the observations (left), and a 60-year segment of CESM2 (right). The observational (CESM2) LIM is trained over the period 1958-2014 (model years 201-1200).

Time series associated with the initial and final optimal structures are computed by projecting the SST and SSH anomaly fields onto those structures. In both observations and CESM2, the initial and final optimal time series are highly correlated (0.75 and 0.73, respectively), with the initial leading the final time series by about 5 months. The large-scale SST, SLP, and precipitation fields concurrent with the initial and final optimal structures are obtained by linearly regressing the SST, SLP, and precipitation fields at each location on the initial and final time series, respectively. The results (Fig. 12) show that the optimal initial structures are associated with SLP dipoles in both the North and South Pacific, which are typical of the North Pacific Oscillation (Rogers, 1981), and the South Pacific Oscillation (You and Furtado, 2017). The equatorward lobes of these SLP patterns are associated with wind anomalies that weaken the climatological trade winds and produce the positive phases of the NPMM and SPMM through reduced latent heat fluxes. SLP anomalies

associated with the optimal final structures are dominated by a deepened and southeastward displaced Aleutian Low in the North Pacific, due to the well-known atmospheric teleconnections of mature El Niño events, a topic further discussed in section 3.5. While the model fidelity in reproducing the large-scale ENSO precursors is overall remarkable, important discrepancies can be seen between the modeled and observed patterns, including, in particular, the excessive amplitude and westward extension of equatorial Pacific SST and precipitation anomalies in the model final fields.

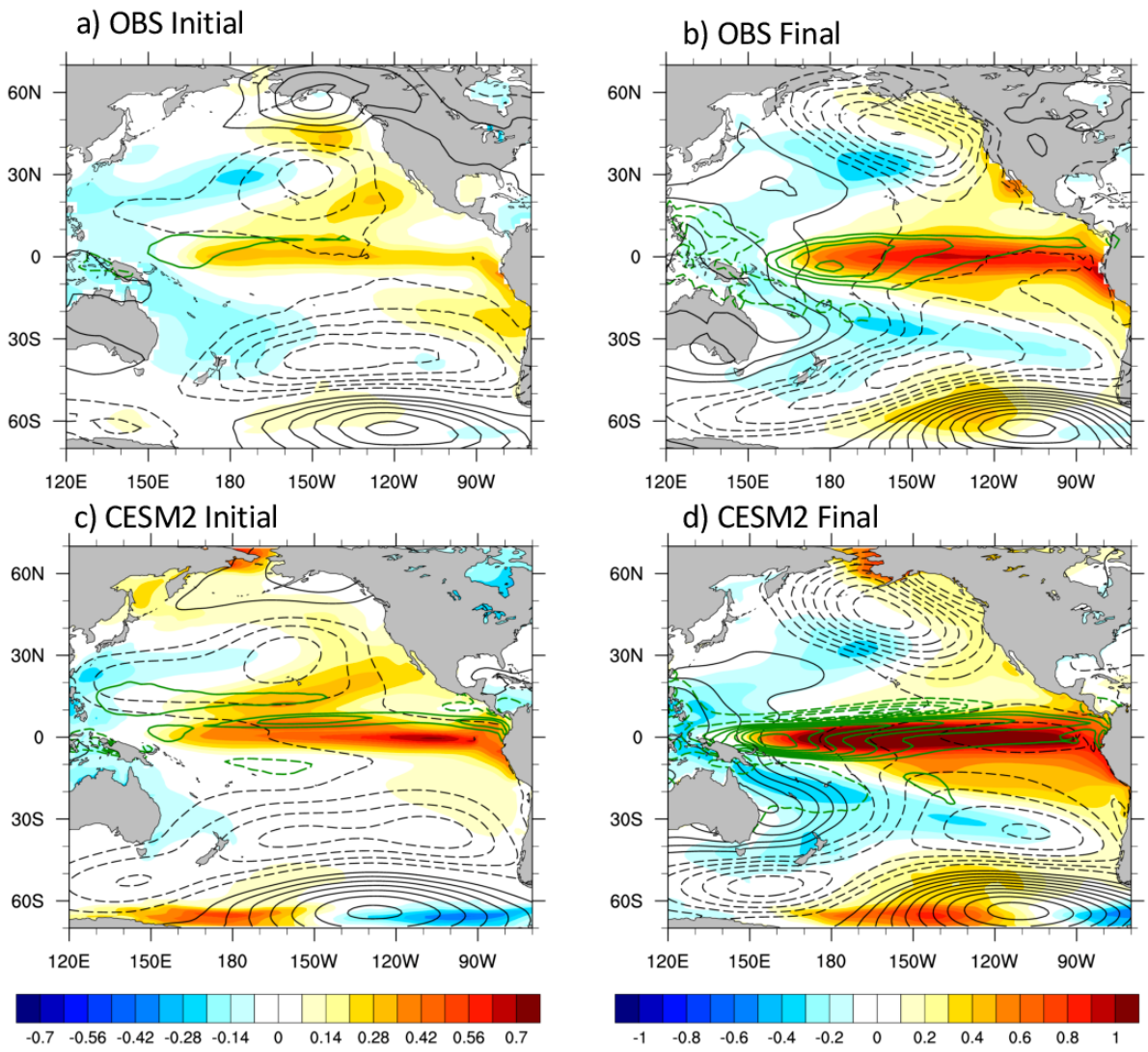

Figure 12. Regressions of SST (shading), SLP (black contours, negative values dashed), and precipitation (green contours, negative values dashed) anomalies upon the initial (left) and final (right) optimal structure indices for (top) observations, and (bottom) CESM2. Observed SST (°C) is from ERSSTv5, SLP (hPa) is from the NCEP/NCAR reanalysis, and precipitation (mm/day) is from the NOAA Precipitation reconstruction for the period 1958-2014. Contour intervals are 0.2 hPa for SLP and 0.5 mm/day for precipitation.

3.4 ENSO diversity

Several different indices have been introduced to characterize diversity in the spatial pattern of ENSO events. Special attention has been devoted to the warm phase of ENSO, since El Niño events exhibit larger variations in their spatial patterns than La Niña events (Kug and Ham, 2011). Here, we adopt the approach introduced by Takahashi et al. (2011) to distinguish between events that have their largest SST anomalies in the far eastern Pacific (E-type) from those with the largest anomalies in the central Pacific (C-type). Following the procedure of Takahashi et al. (2011), we first compute the two leading SST EOFs over the 10°S-10°N tropical Pacific domain, which together explain close to 75% of the SST variance in both observations and CESM2. The spatial pattern of the two leading EOFs over a broader meridional domain is obtained by regressing SST anomalies at each grid point on the corresponding PC timeseries (Figs. 13a, b, c, d). The resulting patterns are similar for observations and model, except for an excessive westward displacement of the SST anomalies in CESM2. Regression of SSH anomalies on the PCs shows a zonal dipole pattern (indicative of a flatter thermocline) for EOF1 in both model and observations, while the SSH pattern associated with EOF2 displays an equatorially symmetric pattern that is reminiscent of equatorial wave signals (Fedorov and Brown, 2009) in observations, but an equatorial asymmetric pattern with an enhanced northern Hemisphere component in CESM2.

We construct the E and C indices as a linear combination of PC1 and PC2, following Takahashi et al. (2011):

$$E = (PC1-PC2)/\sqrt{2}, \quad C = (PC1+PC2)/\sqrt{2},$$

and determine the associated patterns through linear regression of the SST and SSH fields on the E and C indices. In observations, the E mode achieves its largest amplitude in the far eastern equatorial Pacific, with a very deep thermocline near the South American coast, while the C-mode has the largest anomalies just to the east of the dateline, and the largest thermocline depth anomalies between 120° and 150°W. The model displays qualitatively similar patterns, except for the westward displacement of the largest anomalies. Also, while the largest SST anomalies are

weaker for the C-mode relative to the E-mode in observations, they are comparable in magnitude in the model.

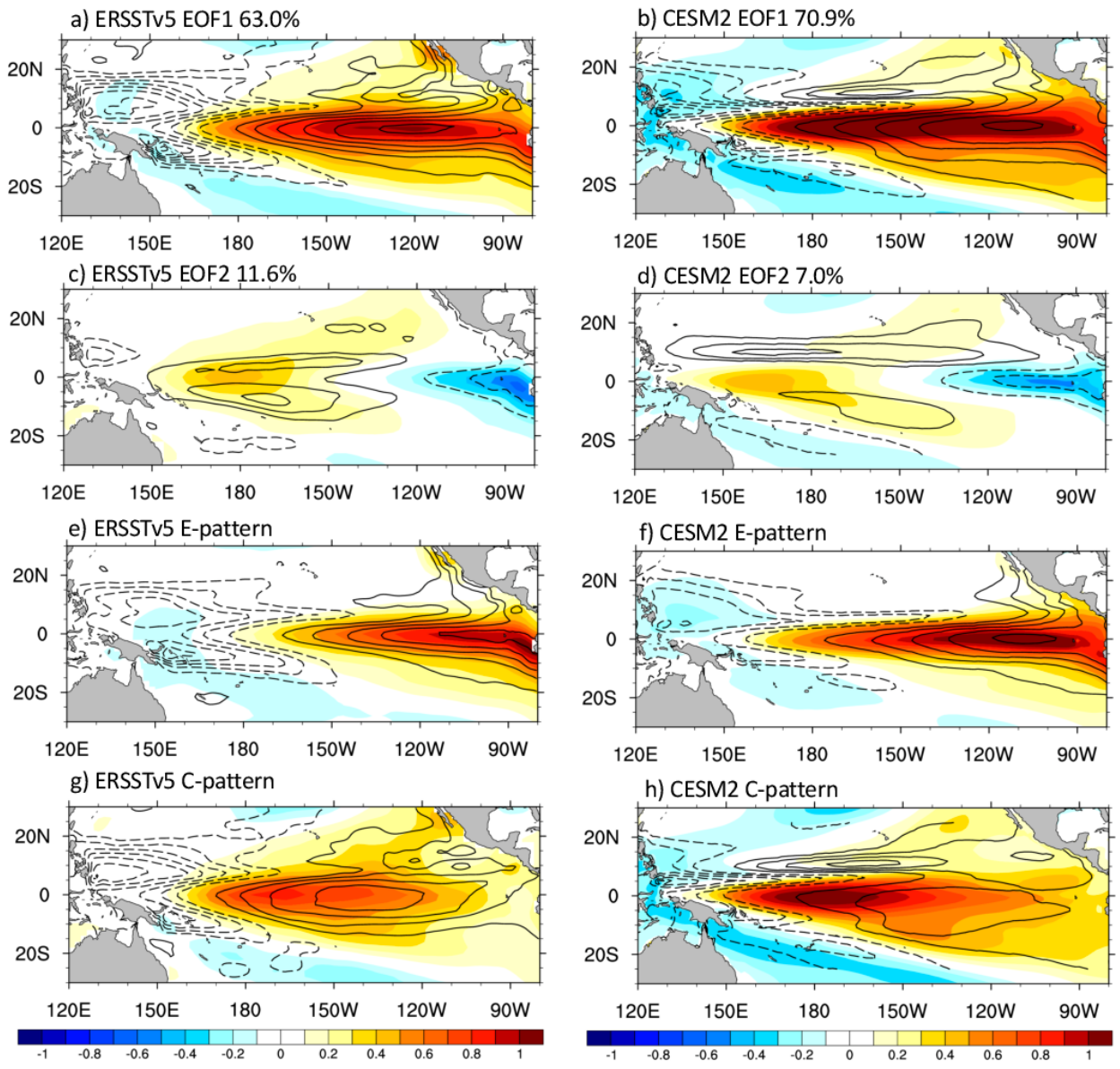

Figure 13. Linear regression of the SST anomalies (°C, shading) and SSH anomalies (cm, contours) on PC1 (top), PC2 (second row), E-index (third row), and C-index (bottom). The observational PCs were obtained from EOF analysis of 1900-2018 ERSSTv5 SST anomalies in the 10°S-10°N tropical Pacific domain, while the CESM2 PCs were computed from EOF analysis of the model SST anomalies over model years 201-1200 over the same 10°S-10°N tropical Pacific domain. SSH observations are from the ORAS4 reanalysis, and the corresponding regressions are based on the 1958-2015 period. Contour interval for SSH is 1 cm. The variance explained by the SST EOFs in the 10°S-10°N domain is shown above the panels displaying the EOF patterns.

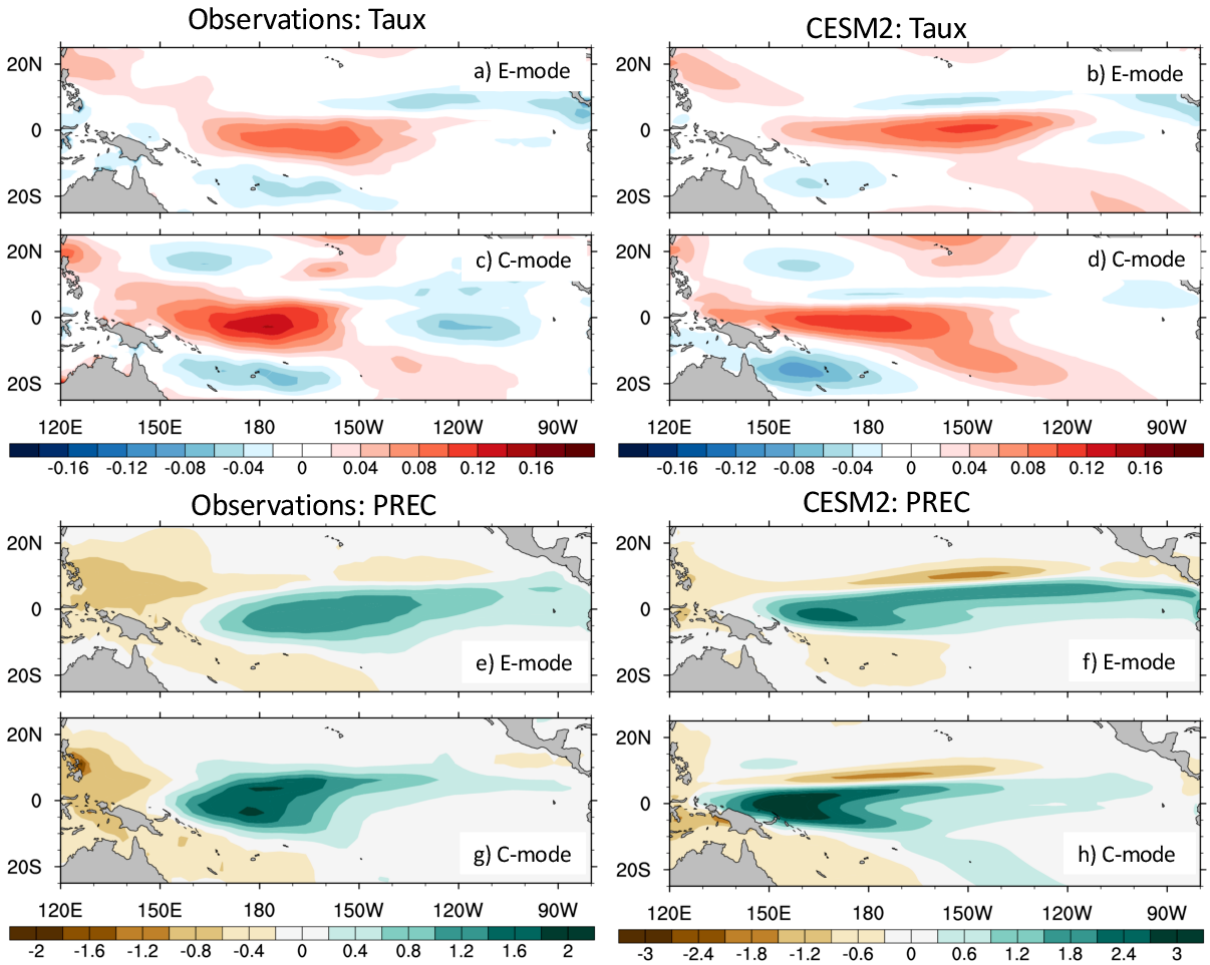

Figure 14. Patterns of anomalous zonal wind stress (panels a-d) and precipitation (panels e-h) associated with the E and C modes for observations (left) and CESM2 (right). The patterns are obtained by linearly regressing the zonal wind stress and precipitation anomalies on the E and C indices. The zonal wind stress (N/m^2) is from the NCEP/DOE reanalysis, and precipitation (mm/day) is from the NOAA Precipitation reconstruction dataset.

Regression of the zonal wind stress and precipitation fields on the E and C indices (Fig. 14) shows that both quantities are confined to the western Pacific for the C-modes in both observations and model, as noted in previous studies of ENSO diversity (Kug et al., 2009; Kug et al., 2010; Capotondi, 2013). This westward confinement is particularly pronounced in CESM2, where the largest precipitation anomalies are found between 150° and 160°E. The largest precipitation anomalies remain localized around the dateline also for the E-mode in CESM2, with only a narrow band just north of the equator extending further east.

3.5 ENSO teleconnections

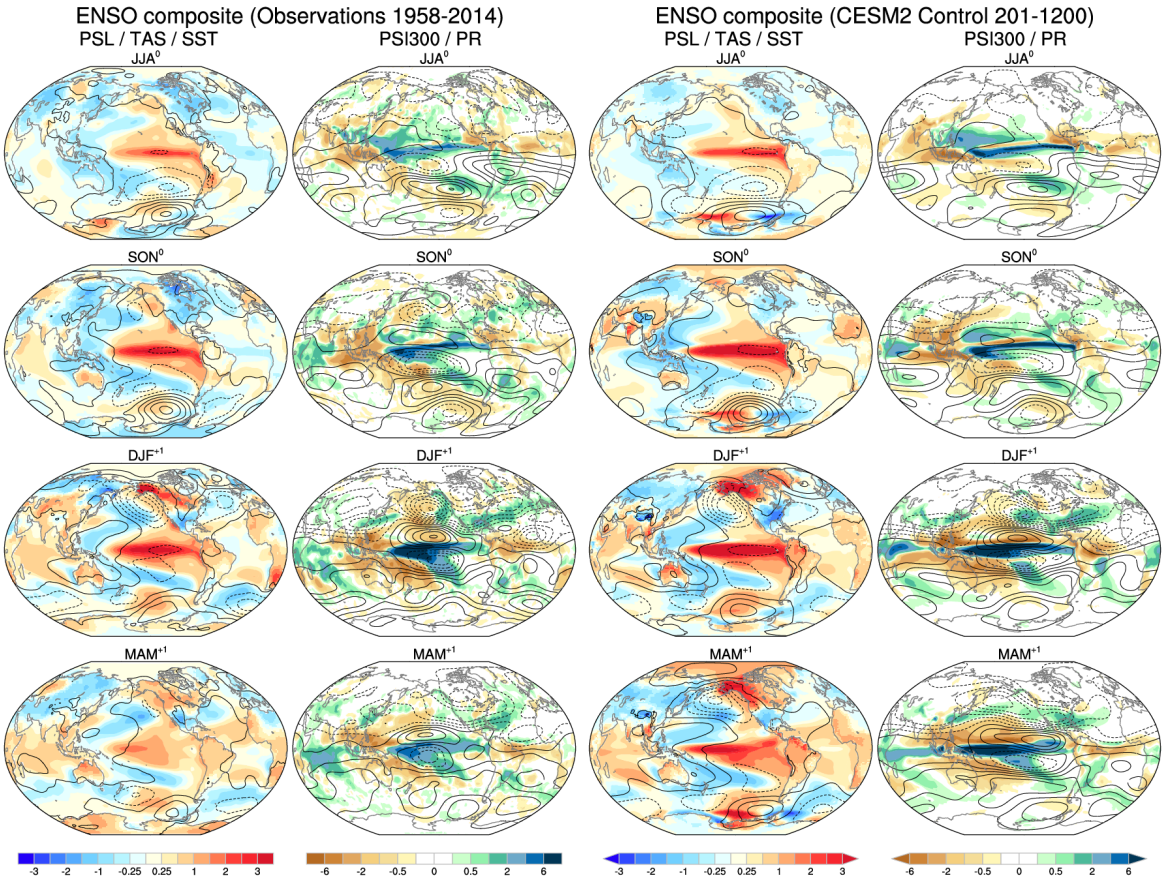

Figure 15. ENSO composite seasonal evolution from (top) JJA (year 0) through (bottom) MAM (year +1) based on observations (left pair of columns) and CESM2 piControl (right pair of columns). The left column of each pair shows SST and terrestrial near-surface air temperature (color shading) and SLP (contours, negative values dashed, contour interval of 2 hPa), and the right column of each pair shows precipitation (mm day^{-1}; color shading) and 300 hPa streamfunction (contours, negative values dashed, contour interval of 3 x 10^6 m^2 s^{-1}) anomalies. The observed composite is based on years 1958–2014 except for precipitation and 300 hPa streamfunction which are for 1979-2014. The CESM2 composite is based on model years 201-1200. See text for details.

Here we provide a more systematic view of global ENSO teleconnections in the CESM2 piControl, along with comparison to observations and the 10-member CAM6 AMIP ensemble. El Niño and La Niña events are defined as in Section 3.2, and ENSO composites are defined as the composite difference between El Niño and La Niña. The seasonal evolution of the observed and CESM2 ENSO composites from June-August of year 0 (JJA^0) through March-May of year +1 (MAM^{+1}) are shown in Fig. 15 for 5 different variables: SLP, 300 hPa streamfunction, SST, near-surface air

temperature and precipitation. Similar ENSO composite maps based on CCSM4 are provided in Deser et al. (2012). Overall, the global patterns of ENSO teleconnections are realistically simulated in CESM2, and are similar to those found in CCSM4 (see Fig. 15 in Deser et al., 2012). In particular, the seasonality and spatial structure of atmospheric circulation anomalies are well reproduced, beginning in JJA^0 with a wave train emanating from the central equatorial Pacific to the South Pacific and followed in DJF^{+1} by a similar Rossby wave train to the North Pacific. Like CCSM4 (and other models: Chen et al., 2019), CESM2 overestimates atmospheric teleconnections in MAM^{+1}, especially those over the North Pacific. This may be associated with the tendency for ENSO SST and precipitation anomalies over the western equatorial Pacific to persist too strongly into boreal spring in the model compared to nature (compare simulated and observed MAM^{+1} panels in Fig. 15). However, the amplitudes of the extra-tropical atmospheric circulation anomalies in other seasons are generally realistic in CESM2 despite the fact that ENSO itself is approximately 30% stronger than observed (recall Section 3.1). We shall return to this point below.

ENSO-related atmospheric teleconnections produce surface climate anomalies through changes in heat and moisture transports. For example, the well-known impacts of ENSO on North American temperature and precipitation in boreal winter are reproduced in CESM2, especially the anomalous warming over western and central Canada and cooling over the southeastern United States, and the increased precipitation over parts of the western and southern United States (Fig. 15, DJF^{+1} panels).

A number of factors hinder a direct comparison of ENSO teleconnections and associated climate impacts between observations and CESM2, including: disparities in the length of record (approximately 56 years for observations and 1200 years for CESM2) and thus the number of ENSO events composited; shortcomings in the model's simulation of ENSO amplitude, pattern and duration; and the fact that the model is run under constant 1850 radiative forcing conditions whereas the real world is subject to evolving radiative forcings. To circumvent these issues, we analyze ENSO composites from the 10-member CAM6 (1-degree) "Tropical Ocean – Global Atmosphere" (TOGA) AMIP ensemble, which is forced at the lower boundary by the observed (ERSSTv5) evolution of SSTs in the tropics (30°N-30°S) from 1920-2014, with SSTs elsewhere set to their long-term mean seasonal cycle, and subject to the observed evolution of historical

radiative forcings (see Deser et al., 2018 for details). The only difference amongst the individual ensemble members is a tiny (order 10^{-14} K) perturbation to the initial atmospheric temperatures on 1 January, 1920, which serves to create ensemble spread due to internal atmospheric variability. Here we compare observed and simulated ENSO composites using the same (observed) set of ENSO events during the extended 1920-2014 period, with a focus on the peak season DJF^{+1}. For this period, we identify 18 El Niño and 14 La Niña events using the procedure outlined in Section 3.2.

Figure 16 shows the DJF^{+1} ENSO composites of SST, terrestrial air temperature and SLP for observations (top left) and each of the 10 CAM6 TOGA AMIP simulations (remaining panels) based on detrended data. Recall that outside the tropics (30°N-30°S), the model generates its own air temperature anomalies (although SST anomalies are identically zero by design). Each simulated ENSO composite shows a center of negative SLP anomalies over the North Pacific with a NW-SE orientation; however, the maximum amplitude of this center varies from approximately 6 hPa (ensemble member #4) to 12 hPa (ensemble member #2). The observed ENSO composite has a similar primary center-of-action, with a peak magnitude of approximately 8 hPa, well within the TOGA ensemble spread. Simulated teleconnections in other parts of the world vary from member to member. For example, the north-south SLP dipole over the North Atlantic, which resembles the North Atlantic Oscillation (NAO), is evident in some members (#2, 8 and 10) but not in others (#1, 3 and 4). This diversity in teleconnection patterns and amplitudes attests to the fact that, even with so many ENSO events, the composites are still subject to considerable sampling uncertainty as a result of strong internally-generated modes of atmospheric circulation variability (see also Deser et al., 2017). This makes it challenging to assess the impact of ENSO diversity and asymmetries on atmospheric teleconnections in the single observational record (see Deser et al., 2017 and 2018 for further discussion).

The range of ENSO teleconnections in the CAM6 TOGA ensemble has implications for the associated surface climate impacts, including air temperature (Fig. 16). For example, positive temperature anomalies over western Canada range from 3°C to over 6°C depending on the influence from residual atmospheric "noise". Similarly, the magnitude of cooling over the southern United States varies from -0.5° C to nearly -4.0° C across the TOGA composites. In both cases,

the model spread encompasses the observed ENSO composite values. Another striking difference across the CAM6 TOGA ensemble is the variation in the sign of the composite air temperature anomalies over northern Asia, which range from -3° C to + 2° C. Again, this variation occurs despite the fact that the ENSO composites are based on a large number of events (18 El Niño and 14 La Niña).

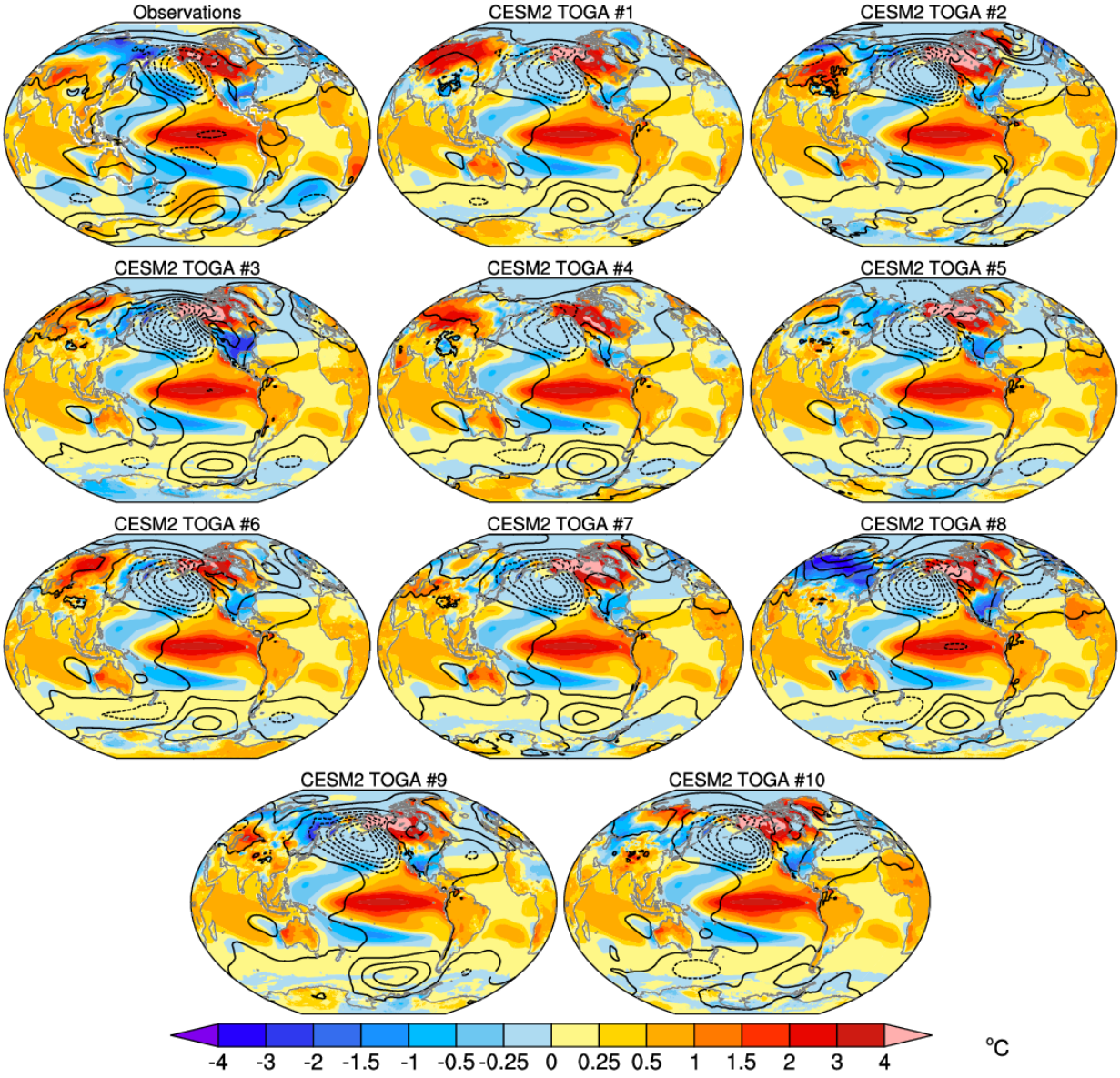

Figure 16. DJF ENSO composites of SST and terrestrial near-surface air temperature (color shading) and SLP (contours, negative values dashed, contour interval of 2 hPa) based on the period 1920-2014 for (top left) observations and (remaining panels) 10 CAM6 TOGA AMIP simulations. See text for details.

4. Pacific Decadal Variability

Although the main focus of this study is on ENSO, here we briefly describe the related phenomenon of PDV (recall Section 1). One way to define PDV is to perform EOF analysis of monthly SST anomalies over the North Pacific (20-60ºN) following Mantua et al. (1997). This "mode of variability" is traditionally termed the "Pacific Decadal Oscillation" (PDO), although as mentioned in the Introduction, we opt for the more general PDV nomenclature. Observed PDV, based on ERSSTv5 over the period 1920-2014, exhibits a basin-wide structure, consisting of SST anomalies of one sign in the central and western North Pacific and the opposite sign along the eastern North Pacific, and is linked to SST anomalies in the tropical and South Pacific reminiscent of the pattern associated with the interannual ENSO phenomenon albeit with weaker amplitude along the equator (Fig. 17, upper left). Observed PDV also has an atmospheric signature, depicted here in terms of regressions of the surface wind field upon the normalized PDV timeseries (Fig. 17, upper left). When PDV is in its positive phase, the Aleutian Low pressure center is deeper than normal, accompanied by westerly wind anomalies over the central and western North Pacific, southerly wind anomalies in the eastern North Pacific, and westerly wind anomalies over the western half of the tropical Pacific. The CESM2 piControl run simulates a realistic spatial pattern of PDV SST and surface wind anomalies throughout the Pacific, including the tropics. Indeed, the match with observations is remarkable, and considerably better than many models including CCSM3 and CCSM4 which lack a strong tropical connection (Deser et al., 2012; Newman et al., 2016).

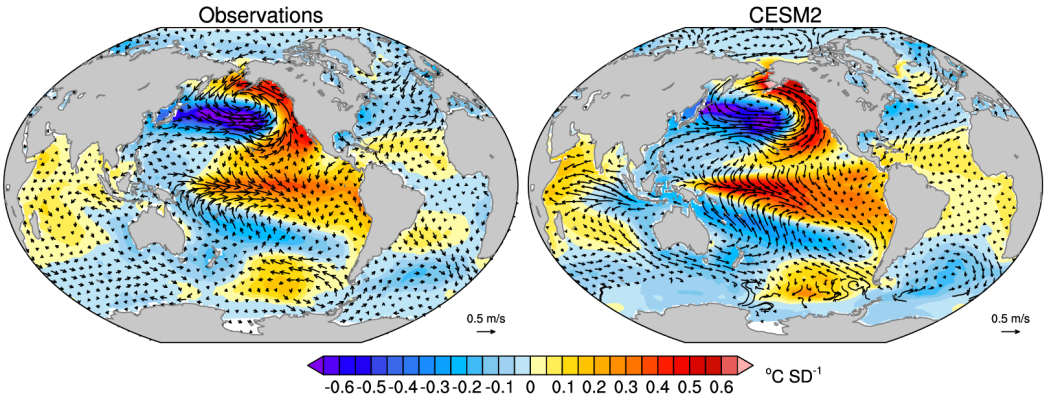

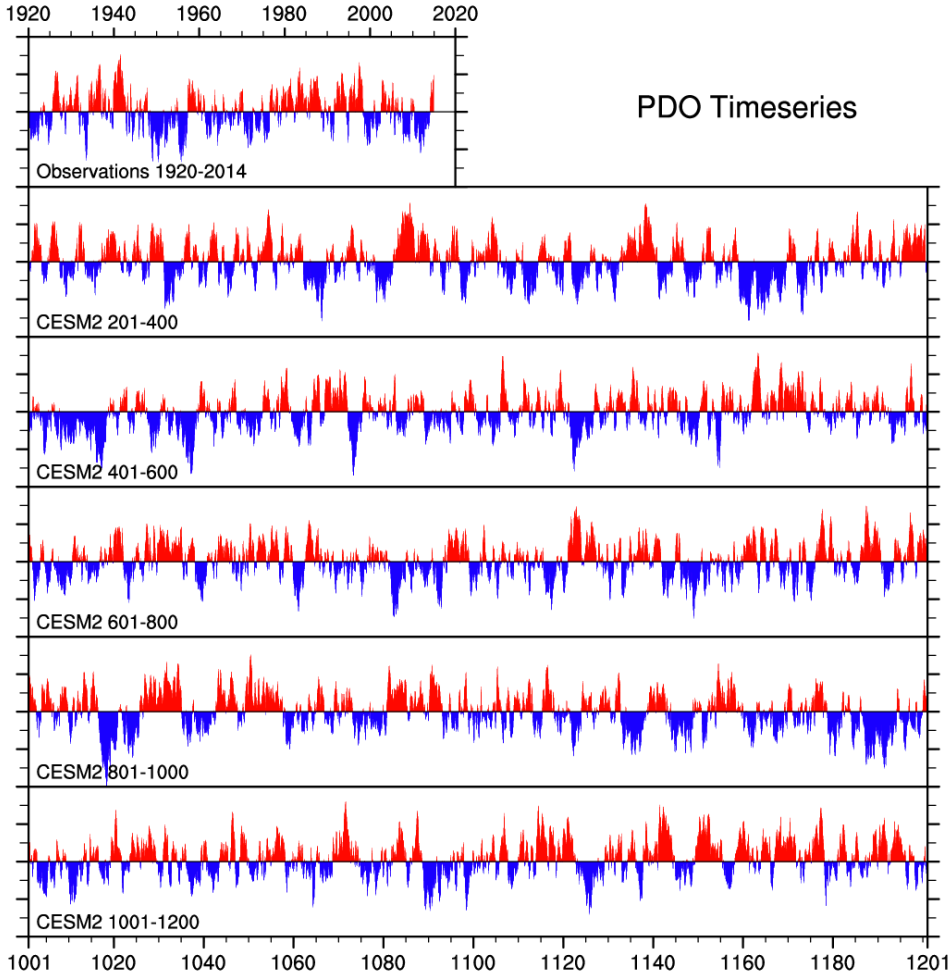

Figure 17. (Top) Spatial pattern and (bottom) temporal evolution of the Pacific Decadal Oscillation (PDO; Mantua et al., 1997) in observations (1920-2014) and the CESM2 piControl simulation (model years 201-1200) based on monthly SST anomalies. Maps show global SST (color shading, °C) and surface wind vector (arrows, ms^{-1}) anomaly regressions upon the normalized PDO time series. Timeseries show the normalized PDO record based on monthly SST anomalies from (top row) observations (1920-2014) and (subsequent rows) sequential 200-year segments of the CESM2 piControl (model years 201-1200). The vertical axis is the same in all timeseries panels.

The observed PDV record (Fig. 17) exhibits a nominal time scale of approximately 50-years, but the limited length of the record precludes attaching any meaningful statistical significance to this value (see related discussion in Deser et al., 2010 and Fedorov et al., 2019). A weak bi-decadal time scale is also evident in the observed PDV record (Minobe, 1999; Deser et al., 2004). In the CESM2 piControl, PDV exhibits a variety of temporal expressions (Fig. 17). Extended periods of 10-20 years in which PDV is in a predominantly positive or negative state are evident at times (for example, model years 360-440 and 815-900), reminiscent of the character of the short observational record. However, there are also long periods in which PDV fluctuates more rapidly. The rich variety of temporal behavior of the simulated PDV is a cautionary tale for the interpretation of the short observational PDV record.

The tropical component of PDV is particularly important, since analyses of observed SSTs for the past century suggest that decadal variability of tropical Pacific climate is associated with a decadal modulation of ENSO (Figs. 18a-e). Here we define the two leading modes of tropical Pacific decadal variability (TPDV) based on EOF analysis of 10-year low-pass filtered SST variability in the tropical Pacific (23.5°S–23.5°N, 120°E–80°W). The leading mode of TPDV (TPDV1) explains 44% of the total decadal variance and exhibits an ENSO-like anomaly pattern (Fig. 18a). This mode represents the tropical component of the basin-wide PDV discussed earlier (Fig. 17). During the positive phase of TPDV1, El Niño events tend to occur more frequently than La Niña events, and vice versa (Fig. 18d), as also suggested by previous studies (Trenberth and Hurrell 1994; Kiem et al. 2003; Verdon and Frank 2006). The leading PC (PC1) is positively correlated ($r = 0.39$) with the relative frequency of El Niño and La Niña events defined as the difference between the fractions of El Niño and La Niña event counts in a moving 10-year window. The second leading mode of TPDV (TPDV2) explains 16% of the total decadal variance and exhibits a zonal dipole pattern in the tropical Pacific, with the western Pacific pole extending into the central-western North Pacific (Fig. 18b). This mode is associated with multidecadal modulations of the ENSO amplitude discussed in previous studies (e.g., Trenberth and Shea 1987; Gu and Philander 1995; Li et al. 2011; McGregor et al. 2010). The second leading PC (PC2) is weakly correlated ($r = 0.20$) with the ENSO amplitude defined as the standard deviation of the monthly Niño-3.4 index in a moving 10-year window (Fig. 18e). The correlations between the PCs and the indices of ENSO

modulation increase if the Hadley Centre Sea Ice and SST dataset (Rayner et al., 2003) is used instead of the ERSSTv5 dataset (r=0.43 and 0.41 for PC1 and PC2, respectively).

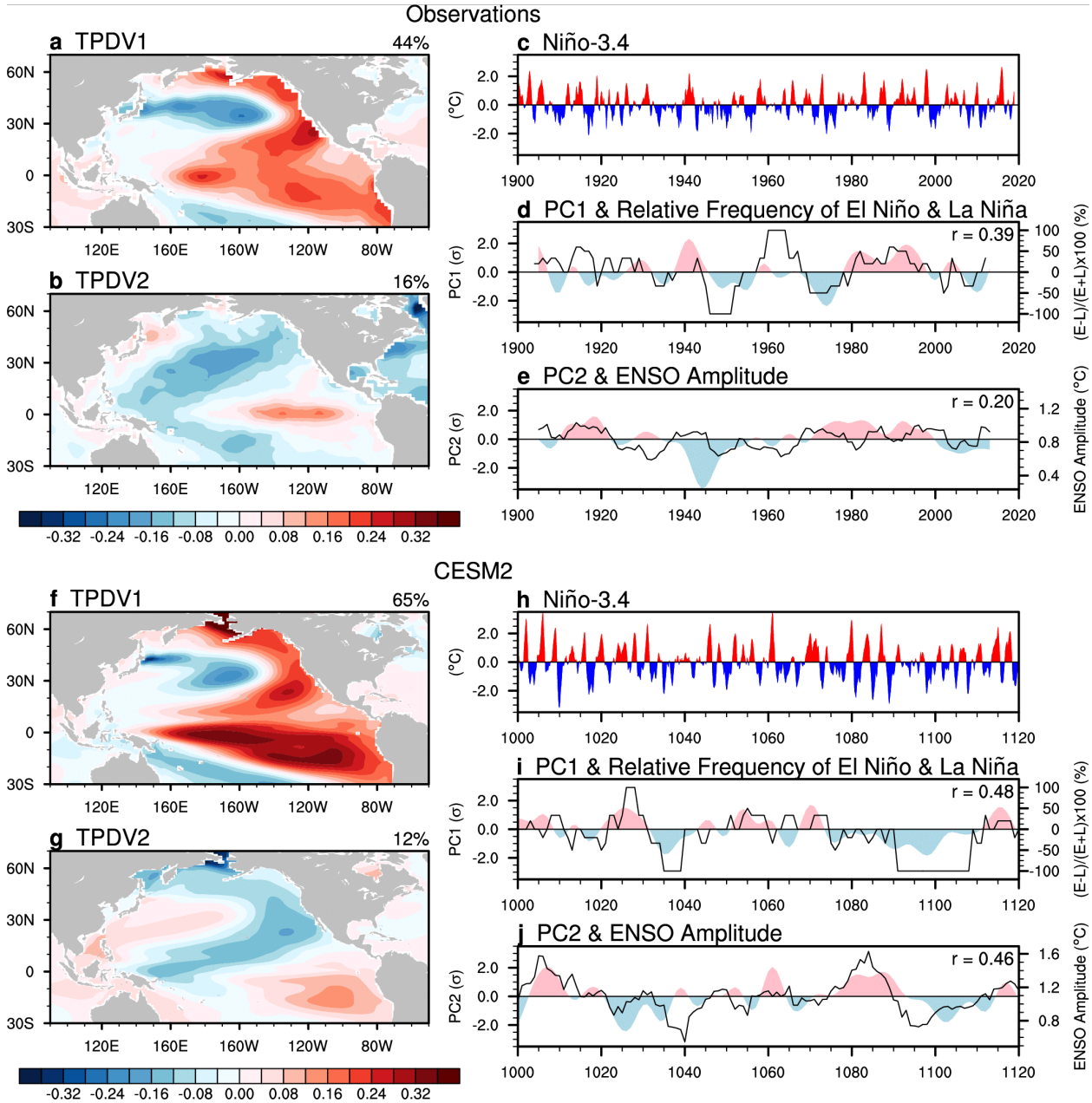

Figure 18. TPDV and ENSO modulations in (a-e) observations (ERSSTv5 over 1900-2018) and (f-j) CESM2 (model years 201-1200). (a) SST anomaly pattern associated with TPDV1 obtained by regressing SST anomalies onto the standardized PC1 of 10-year low-pass filtered SST variability in the tropical Pacific (23.5°S–23.5°N, 120°E–80°W). The fraction of total decadal variance explained by this mode is indicated in the top right. (b) As in (a) but for TPDV2. (c) Time series of the monthly Niño-3.4 index smoothed with a 3-month binomial filter (°C). (d) Time series of PC1 (standard deviation units; shaded curve) and the relative frequency of El Niño and La Niña

events (%; black curve) defined as (E −L)/(E + L) × 100, where E and L are the numbers of El Niño and La Niña events in a moving 10-year window, respectively. El Niño and La Niña events are defined as in Figs. 6 and 7, although consecutive El Niño or La Niña years are counted separately. The correlation coefficient of these time series is indicated in the upper right. (e) As in (d) but for PC2 and the ENSO amplitude (°C) defined as standard deviation of the Niño-3.4 index in a moving 10-year window. (f-j) As in (a-e) but for CESM2. Both observed and CESM2 SST data are linearly detrended prior to the analysis.

While the brevity and uncertainty of observational records make it difficult to assess the robustness of the relationships between TPDV and ENSO modulations, the observed relationships are surprisingly well reproduced in the 1200-year CESM2 piControl run (Fig. 18f-j). Compared to observations, TPDV1 simulated in CESM2 explains a much larger fraction of the total decadal variance (65%) and shows larger SST anomalies in the equatorial and southeastern tropical Pacific (Fig. 18f), presumably related to the excessively strong ENSO in this model (Fig. 1). SST anomalies associated with TPDV2, on the other hand, show a more meridionally symmetric pattern in the central-eastern tropical Pacific (Fig. 18g). It is also interesting to note that the North Atlantic SST anomalies seen in the observed TPDV2 are absent in CESM2. The PC1 and PC2 are significantly correlated with the relative frequency of El Niño and La Niña events (r=0.48) and the ENSO amplitude (r= 0.46), respectively. Similar patterns of the TPDV modes and their relationships to ENSO modulations are found in CCSM4 (Okumura et al. 2017) and CESM1 (not shown). Compared to CESM2 and CESM1, TPDV2 simulated in CCSM4 explains a larger fraction of the total decadal variance (22%) and PC2 is more highly correlated with the ENSO amplitude (r=0.79).

The causality of TPDV and ENSO modulations remains unclear [see a recent review by Fedorov et al. (2019)]. In one view, mean state changes associated with TPDV affect ENSO by modulating the oceanic and atmospheric feedbacks (Fedorov and Philander 2000; Wang and An 2002; Kang et al. 2014; Capotondi and Sardeshmukh 2017; Hu and Fedorov 2018; Sun and Okumura 2019). In another view, ENSO modulations are stochastically forced or internally generated, and the resultant nonzero residuals induce changes in the mean state (Flügel and Chang 1999; Thompson and Battisti 2001; Rodgers et al. 2004; Wittenberg et al. 2014; Atwood et al. 2017). For example, a random increase in the relative frequency of El Niño would result in El Niño-like changes in the mean state. A random increase in the amplitude of ENSO would, on the other hand, induce a zonal

dipole pattern of mean SST changes due to the asymmetry in the El Niño and La Niña SST anomaly patterns. Further studies are needed to understand the origins of TPDV and to what degree TPDV interacts with the ENSO dynamics.

5. Conclusions

In this paper we have provided an overview of ENSO and PDV in the NCAR Community Earth System Model version 2 (CESM2), focusing primarily on the 1200-yr preindustrial integration. ENSO is a coupled ocean-atmosphere phenomenon, and its evolution involves both predictable oceanic processes and stochastic influences from within and outside the tropical Pacific. This complexity of influences and feedbacks results in a large diversity of ENSO spatial patterns and temporal evolutions which are very challenging for climate models to simulate realistically. CESM2 exhibits realistic spectral characteristics, with a dominant timescale very close to the observed, an aspect that appears to be related to the spatial structure of the wind stress response to the ENSO SST anomalies. Indeed, the longitudinal location and meridional scale of the wind stress anomalies are very similar to those found in observations, and can be expected to lead to an adjustment timescale of the equatorial thermocline also similar to the observed. The evolution of the equatorial Warm Water Volume, as described by the leading modes of sea surface height variability appears to be very realistic, and consistent with the Recharge Oscillator paradigm (Jin, 1997). Also, in agreement with recent observational findings, the heat content in the western-to-central Pacific during spring exhibits an asymmetric relationship with ENSO conditions during the following winter, with La Niña events usually following a discharged state and El Niño events being mostly associated with neutral spring conditions. CESM2 also shows a realistic asymmetry in the evolution and duration of warm and cold events, with El Niño events typically transitioning to a La Niña event after their peak, and La Niña events tending to re-occur for a second year, although not as frequently as in the observations.

Extra-tropical ENSO precursors are also well-simulated in CESM2, including the North and South Pacific Meridional Modes, and their associated atmospheric circulation anomalies. CESM2 simulates some degree of diversity in the spatial patterns of El Niño events, with some events exhibiting large anomalies that extend to the eastern equatorial Pacific, and another class of events

characterized by anomalies that are more confined to the central Pacific. As in observations, these two classes of events are associated with different patterns of wind stress and precipitation anomalies, which are more confined to the western part of the basin in the case of the Central Pacific events.

One main limitation in the CESM2 ENSO simulation is its excessive amplitude, which in the Niño-3.4 region is about 30% larger than the observed in the preindustrial simulation and 40% larger in the historical runs, as estimated from the magnitude of the Niño-3.4 spectral peak. Estimates of uncertainty associated with the high level of system noise help to partly reconcile the discrepancy in the spectral power of model and observations, highlighting the strong limitation of relying on the relatively short and uncertain instrumental record to assess model performance.

A second important limitation of the ENSO representation in CESM2 is the excessive westward extension of the ENSO-related SST anomalies, whose maximum standard deviation occurs near the dateline. This also limits the range of ENSO spatial patterns, which are all shifted further west than observed, and the ability of convection to shift as far eastward as observed. The intensity of the eastern Pacific cold tongue is critical to determine how readily deep convection can shift eastward. Since anomalous convective activity depends on the local total SST relative to the tropical mean SST (He et al., 2018), an excessive cold tongue may impede the eastward displacement of deep convection (and precipitation) even in the presence of large SST anomalies. While CESM2 appears to have a reduced cold tongue bias relative to previous model versions, its zonal mean SST is higher than in CESM1 and CCSM4, establishing a higher convective threshold which may be responsible for the westward confinement of precipitation in the model.

In spite of the above limitations, global ENSO teleconnections are reasonably well represented in CESM2 relative to observations, including pattern and seasonality, although a definitive assessment of the model performance is limited by many factors, the most prominent of which is the large level of atmospheric noise. CESM2 also has a pattern of PDV that compares extremely well with the observed. The tropical signature of PDV shows a realistic association with ENSO decadal modulation, although the exact mechanisms underlying this relationship are still unclear and a subject of active research.

Several aspects of ENSO remain to be investigated in the model. Apart from the "deterministic" wind stress response to eastern Pacific SST anomalies, tropical wind stress anomalies also include a stochastic component which appears to play an important role in the onset and magnitude of ENSO events (Puy et al., 2019; Capotondi et al., 2018). The model representation of the stochastic wind component should be examined in detail in future studies. Similarly, additional analyses are needed to understand the influence of sub-seasonal wind variations, e.g., those associated with the Madden-Julian Oscillation on the onset of El Niño events. The mechanisms underlying asymmetric ENSO behavior (e.g., duration of warm and cold ENSO events, state-dependence of stochastic wind forcing) also deserve further investigation. Finally, while the large level of atmospheric noise greatly limits our ability to detect differences in the impact of different ENSO flavors, large ensembles and novel diagnostic approaches should be considered to maximize the value of the model ENSO as a predictor of global impacts.

Acknowlegments

The CESM project is supported primarily by the National Science Foundation (NSF). This material is based upon work supported by the National Center for Atmospheric Research, which is a major facility sponsored by the NSF under Cooperative Agreement No. 1852977. Computing and data storage resources, including the Cheyenne supercomputer (doi:10.5065/D6RX99HX), were provided by the Computational and Information Systems Laboratory (CISL) at NCAR. We thank all the scientists, software engineers, and administrators who contributed to the development of CESM2. Observational datasets for SST, SLP, surface wind stress, and precipitation are available from the NOAA/ESRL/PSD website (https://www.esrl.noaa.gov/psd). The output of the ORAS4 ocean reanalysis was obtained from http://icdc.cen.uni-hamburg.de/projekte/easy-init/esy-init-ocean.html. The Authors declare no conflict of interest.

References

Adler, R. F., et al. (2003). The Version-2 Global Precipitation Climatology Project (GPCP) monthly precipitation analysis (1979-present). J. Hydrometeor., 4, 1147-1167.

Alexander, M.A, Deser, C. & Timlin, M.S. (1999). The reemergence of SST anomalies in the North Pacific Ocean. J. Climate, 12, 2419-2431.

Alexander, M. A., Vimont, D. J., Chang, P. & Scott, J. D. (2010). The impact of extratropical atmospheric variability on ENSO: Testing the seasonal footprinting mechanism using coupled model experiments. J. climate, 23, 2885-2901.

Atwood, A. R., Battisti, D. S., Wittenberg, A. T., Roberts, W. H. G., & Vimont, D. J. (2017). Characterizing unforced multi-decadal variability of ENSO: A case study with the GFDL CM2.1 coupled GCM. *Climate Dynamics.* 49(7-8), 2845–2862.

Anderson, B.T., Perez, R. & Karspeck, A. (2013). Triggering of El Niño onset through the trade wind – induced charging of the equatorial Pacific. Geophys. Res. Lett., 40, 1212-1216.

An, S.-I., & Wang, B. (2000). Interdecadal change of the structure of the ENSO mode and its impact on the ENSO frequency. J. Climate, 13, 2044-2055.

An, S.-I., Tziperman, E., Okumura, Y., & Li, T. (2019). ENSO irregularity and asymmetry. El Niño-Southern Oscillation in a Changing Climate, Geophysical Monograph, American Geophysical Union, in press.

Ashok, K., Behera, S.K., Rao, S.A., Weng, H., & Yamagata, T. (2007). El Niño Modoki and its possible teleconnections. *J. Geophys. Res*., **112**, C11007, doi:10.1029/2006JC003798

Balmaseda. M.A., Mogensen, K. & Weaver, A.T. (2013). Evaluation of the ECMWF ocean reanalysis system ORAS4. Q. J. R. Meteorol. Soc., 139, 1132-1161.

Barsugli, J.j., & Sardeshmukh, P.D. (2002). Global atmospheric sensitivity to tropical SST anomalies throughout the Indo-Pacific basin. *J. Climate*, **15**, 3427-3442.

Bayr, T., Latif, M., Dommenger, D., Wengel, C., Harlaß, J., Park, W. (2018). Mean-state dependence of ENSO atmospheric feedbacks in climate models. *Climate Dynamics.* 50, 3171–3194.

Bellenger, H., Guilyardi, E., Leloup, J., Lengaigne, M., & Vialard, J. (2014). ENSO representation in climate models: from CMIP3 to CMIP5. *Clim. Dyn*., **42**, 1999-2018.

Cai, W. et al. (2019). Pantropical climate interactions. Science, 363, doi:10.1126/science.aav4236.

Capotondi, A. (2013). ENSO diversity in the NCAR CCSM4 climate model. J. Geophys. Res., 118, 4755-4770, doi:10.1002/jgrc.20335.

Capotondi, A., Wittenberg, A.T., & Masina, S. (2006). Spatial and temporal structure of tropical Pacific interannual variability in 20th century climate simulations. *Ocean Modelling*, **15**, 274-298.

Capotondi, A., et al. (2015a). Understanding ENSO Diversity. *Bull. Amer. Meteor. Soc.*, **96**, 921-938.

Capotondi, A., Y.-G. Ham, A. T. Wittenberg, and J.-S. Kug (2015b), Climate model biases and El Niño Southern Oscillation (ENSO) simulation, *US CLIVAR Variations*, **13**(1), 21-25.

Capotondi, A.& Sardeshmukh, P.D. (2017). Is El Niño *really* changing? Geophys. Res. Lett., 44, 8548–8556. doi:10.1002/2017GL074515

Capotondi, A., Sardeshmukh, P. D. & Ricciardulli, L. (2018). The nature of the stochastic wind forcing of ENSO. J. Climate, 31, 8081-8099.

Capotondi, A., Sardeshmukh, P.D., Di Lorenzo, E., Subramanian, A., & Miller, A.J. (2019). Predictability of US West Coast Ocean Temperatures is not solely due to ENSO. *Scientific Reports*, **9**:10993, https://doi.org/10.1038/s41598-019-47400-4.

Capotondi, A., Wittenberg, A.T., Kug, J.-S., Takahashi, K., & McPhaden, M.J. (2019). ENSO Diversity. AGU Monograph "El Niño Southern Oscillation in a Changing Climate", A. Santoso, M. McPhaden & W. Cai, Editors, in press.

Chen, R., I. R. Simpson, C. Deser, W. Huang and B. Wang, 2020: Model biases in the simulation of the springtime North Pacific ENSO 2 teleconnection. To be submitted to *J. Climate* in early January 2020.

Chiang, J.C.H., & Vimont, D. J. (2004). Analogous Pacific and Atlantic meridional modes of tropical atmosphere.ocean variability. *J. Climate*, **17**, 4143-4158

Danabasoglu, G. et al. (2019). The Community Earth System Model version 2 (CESM2). JAMES, submitted.

Dee, D. P. et al. (2011). The ERA-Interim reanalysis: Configuration and performance of the data assimilation system. Quart. J. Roy. Meteor. Soc., 137, 553-597.

Deser, C., Phillips, A.S. & Hurrell, J.W. (2004). Pacific interdecadal climate variability: Linkages between the tropics and the North Pacific during boreal winter since 1900. J. Climate, 17, 3109-3124.

Deser, C., M. A. Alexander, S. -P. Xie, and A. S. Phillips, 2010: Sea surface temperature variability: patterns and mechanisms. *Ann. Rev. Mar. Sci.*, **2010.2**, 115-143, doi:10.1146/annurev-marine-120408-151453.

Deser, C., Phillips, A.S., Tomas, R.A., Okumura, Y. M., Alexander, M.A., Capotondi, A., Scott, J. D., Kwon, Y.-O., & Ohba, M. (2012). ENSO and Pacific Decadal Variability in the Community Climate System Model Version 4. *J. Climate*, **25**, 2622-2651.

Deser, C., I. R. Simpson, K. A. McKinnon and A. S. Phillips, 2017: The Northern Hemisphere extra-tropical atmospheric circulation response to ENSO: How well do we know it and how do we evaluate models accordingly? *J. Climate*, **30**, 5059-5082, doi: 10.1175/JCLI-D-16-0844.1.

Deser, C., Simpson, I.R., Phillips, A.S., & McKinnon, K.A. (2018). How well do we know ENSO's climate impacts over North America, and how do we evaluate models accordingly? *J. Climate*, **30**, 4991-5014.

Dewitte, B., et al. (2012). Change in El Niño flavours over 1958-2008: Implications for the long-term trend of the upwelling off Peru. Deep-Sea Res. II, 77-80, 143-156.

DiNezio, P., C. Deser, A. Karspeck, S. Yeager, Y. Okumura, G. Danabasoglu, N. Rosenbloom, J. Caron and G. A. Meehl (2017a). A two-year forecast for a 60-80% chance of La Niña in 2017-18. *Geophys. Res. Lett.*, **44**, 11624–11635, doi: 10.1002/2017GL074904.

DiNezio, P. N., Deser, C., Okumura, Y., & Karspeck, A. (2017b). Predictability of 2-year La Niña events in a coupled general circulation model. *Climate Dynamics.* 49(11), 4237–4261.

Dommenget, D., Bayr, T., & Frauen, C. (2013). Analysis of the nonlinearity in the pattern and time evolution of El Niño Southern Oscillation. *Climate Dynamics.* 40(11), 2825–2847.

Fedorov, A. & Philander, S.G. (2000). Is El Niño changing? Science, 288, 1997-2002.

Gent, P.R. et al. (2011). The Community Climate System Model version 4. J. Climate, 24, 4973-4991.

Fedorov, A. V. & Brown, J. (2009). Equatorial waves. In "Encyclopedia of Ocean Sciences (Second Edition), J. Steele, Ed., Academic Press, 3679-3695.

Fedorov, A., Hu, S., Wittenberg, A., Levine, A., & Deser, C., (2019). ENSO low-frequency modulations and mean state interactions. ENSO in a Changing Climate, M. McPhaden. A. Santoso and W. Cai, Eds., AGU Monograph, in press.

Flügel, M., & Chang, P. (1999). Stochastically induced climate shift of El Niño-Southern Oscillation. *Geophysical Research Letters.* 26(16), 2473–247.

Gierach, M.M., Lee, T., Turk, D., & McPhaden, M.J. (2012). Biological response to the 1997-98 and 2009-10 El Niño events in the equatorial Pacific Ocean. *Geophys. Res. Lett.*, **39**, L10602, doi:10.1029/2012GL051103.

Glantz, M.H. (2000). Currents of Change: El Niño and La Niña impacts on climate and society. Cambridge University Press, 252 pp.

Golaz, J.-C., Larson, V.E. & Cotton, W.R. (2002). A PDF-based model for boundary layer clouds. Part I: Merthod and model description. J. Atmos. Sci., 59, 3540-3551.

Gu, D., & Philander, S. (1995). Secular changes of annual and interannual variability in the tropics during the past century. *Journal of Climate.* 8(4), 864–876.

Guilyardi, E., Bellenger, H., Collins, M., Ferrett, S., Cai, W., & Wittenberg, A.T. (2012). A first look at ENSO in CMIP5. *CLIVAR Exchanges*, **17**, 29-32. ISSN: 1026-0471

Ham, Y.-G., and J.-S. Kug (2012), How well do current climate models simulate two types of El Niño?, *Clim. Dyn.*, **39**, 383-398.

He, J., N. C. Johnson, G. A. Vecchi, B. Kirtman, A. T. Wittenberg, and S. Sturm (2018), Precipitation sensitivity to local variations in tropical sea surface temperature. *J. Climate*, **31** (22), 9225-9238. doi:10.1175/JCLI-D-18-0262.1

Hersbach, H., et al. (2019). Global reanalysis: goodbye ERA-Interim, hello ERA5. ECMWF Newsletter No. 159, 17-24, doi:10.21957/vf291hehd7.

Hu, S., & Fedorov, A. V. (2018). Cross-equatorial winds control El Niño diversity and change. *Nature Climate Change.* 8(9), 798–802.

Huang, B., et al. (2017). Extended Reconstructed Sea Surface Temperature version 5 (ERSSTv5): Upgrades, validations, and intercomparisons. *J. Climate*, 30, 8179-8205.

Hurrell, J.W. et al. (2013). The Community Earth System Model: A framework for collaborative research. Bull. Amer. Meteor. Soc., 94, 1339-1360.

Izumo, T., Lengaigne, M., Vialard, J., Suresh, I. & Planton, Y. (2019). On the physical interpretation of the lead relation between Warm Water Volume and the El Niño Southern Oscillation. Clim. Dyn., 52, 2923-2942.

Jin, F.-F. (1997). An equatorial ocean recharge paradigm for ENSO. Part I: conceptual model. J. Atmos. Sci., 54, 811-829.

Johnson, N. C., & Kosaka, Y. (2016). The impact of eastern equatorial Pacific convection on the diversity of boreal winter El Niño teleconnection patterns. *Climate Dynamics.* 47, 3737–3765.

Kalney, E., et al. (1996). The NCEP/NCAR 40-year reanalysis project. Bull. Amer. Meteor. Soc., 77, 437-471.

Kanamitsu, M., Ebisuzaki, W., Woollen, J., Yang, S.-K., Hnilo, J. J., Fiorino, M. & Potter, G. L. (2002). NCEP-DOE AMIP-II Reanalysis (R-2). Bull. Amer. Meteor. Soc., 83, 1631-1643.

Kang, I.-S., No, H.-H., & Kucharski, F. (2014). ENSO amplitude modulation associated with the mean SST changes in the tropical central Pacific induced by Atlantic multidecadal oscillation. *Journal of Climate.* 27(20), 7911–7920.

Kiem, A. S., Franks, S. W., & Kuczera, G. (2003). Multi-decadal variability of flood risk. *Geophysical Research Letters.* 30(2), 1035, doi: 10.1029/2002GL015992.

Kirtman, B.P. (1997). Oceanic Rossby wave dynamics and the ENSO period in a coupled model. J. Climate, 10, 1690-1704.

Kug, J.-S., Jin, F.-F. & An, S.-I. (2009). Two types of El Niño events: Cold tongue El Niño and Warm Pool El Niño. J. Climate, 22, 1499-1515.

Kug, J.-S. et al. (2010). Warm Pool and Cold Tongue El Niño events as simulated by the GFDL 2.1 coupled GCM. J. Climate, 23, 1226-1239.

Kug, J.-S. & Ham, Y.-G. (2011). Are there two types of La Niña?, *Geophys. Res. Lett.*, **38**, doi:10.1029/2011GL048237.

Kug, J.-S., Y.-G. Ham, J.-Y. Lee, and F.-F. Jin (2012), Improved simulation of two types of El Niño in CMIP5 models, *Environ. Res. Lett.* , **7**, doi:10.1088/1748-9326/3/034002.

Kwon, Y.-O. & Deser, C. (2007). North Pacific decadal variability in the Community Climate System Model version 2. J. Climate, 20, 2416-2433.

Larkin, N. K., & Harrison, D. E. (2002). ENSO warm (El Niño) and cold (La Niña) event life cycles: Ocean surface anomaly patterns, their symmetries, asymmetries, and implications. *Journal of Climate.* 15(10), 1118–1140.

Larkin, N. K., & Harrison, D.E. (2005). On the definition of El Niño and associated seasonal average U.S. weather anomalies. *Geophys. Res. Lett.*, **32**, L13705, doi:10.1029/2005GL022738.

Larson, S. M., Pegion, K.V. & Kirtman, B. P. (2018). The South Pacific Meridional Mode as a thermally driven source of ENSO amplitude modulation and uncertainty. J. Climate, 31, 5127-5145.

Larson, S.M. & Pegion, K. V. (2019). Do Asymmetries in ENSO predictability arise from different recharge states? Clim. Dyn., Revised.

Larson, S. M. & Kirtman, B. P. (2019). Linking preconditioning to extreme ENSO events and reduced ensemble spread. *Clim. Dyn.*, **52**, 7417–7433, https://doi.org/10.1007/s00382-017-3791-x.

Lee, K.-W., Yeh, S.-W., Kug, J.-S. & Park, J.-Y. (2014). Ocean Chlorophyll response to two types of El Niño events in an ocean-biogeochemical coupled model. J. Geophys. Res., 119, 933-952.

Li, J., Xie, S.-P., Cook, E. R., Huang, G., D'Arrigo, R., Liu, F., Ma, J., & Zheng, X.-T. (2011). Interdecadal modulation of El Niño amplitude during the past millennium. *Nature Climate Change.* 1(2), 114–118.

Li, Q., Webb, A., Fox-Kemper, B., Craig, A., Danabasoglu, G., Large, W.G. & Vertenstein, M. (2016). Langmuir mixing effects on global climate: WAVEWATCH III in CESM. Ocean Modeling, 103, 145-160.

Mantua. N.J., Hare, S.R., Zhang, Y., Wallace, J.M. & Francis, R.C. (1997). A Pacific interdecadal oscillation with impacts on salmon production. Bull. Amer. Meteor. Soc., 78, 1069-1079.

McGregor, S., Timmermann, A., & Timm, O. (2010). A unified proxy for ENSO and PDO variability since 1650. *Climate of the Past.* 6(1), 1–17.

McGregor, S., Timmermann, A., Jin, F.-F. & Kessler, W. S. (2016) Charging El Niño with off-equatorial westerly wind events. *Clim. Dyn.*, **47**, 1111–1125, https://doi.org/10.1007/s00382-015-2891-8.

McPhaden, M.J., Zebiak, S.E., & Glantz, M.H. (2006). ENSO as an intriguing concept in Earth science. *Science*, **314**, 1740-1745.

Meinen, C.S. & McPhaden, M.J. (2000). Observations of warm water volume changes in the equatorial Pacific and their relationship to El Niño and La Niña. J. Climate, 13, 3551-3559.

Neale, R.B., Richter, J.H., &Jochum, M. (2008). The impact of convection of ENSO: From a delayed oscillator to a series of events. *J. Climate*, **21**, 5904-5924.

Neske, S. & McGregor, S. (2018). Understanding the Warm Water Volume precursor of ENSO events and its interdecadal variation. *Geophys. Res. Lett.*, **45**, 1577–1585, https://doi.org/10.1002/2017GL076439.

Newman, M., Alexander, M.A. & Scott, J.D. (2011). An empirical model of tropical ocean dynamics. Clim. Dyn., 37, 1823-1841.

Newman, M. et al. (2016). The Pacific Decadal Oscillation, revisited. J. Climate, 29, 4399-4427.

Ohba, M., & Ueda, H. (2009). Role of nonlinear atmospheric response to SST on the asymmetric transition process of ENSO. *Journal of Climate.* 22(1), 177–192.

Okumura, Y. M. (2019). ENSO diversity from an atmospheric perspective. *Current Climate Change Report.* 5(3), 245-257.

Okumura, Y. M., & Deser, C. (2010). Asymmetry in the duration of El Niño and La Niña. *Journal of Climate.* 23(21), 5826–5843.

Okumura, Y. M., Sun, T., & Wu, X. (2017). Asymmetric modulation of El Niño and La Niña and the linkage to tropical Pacific decadal variability. *Journal of Climate.* 30(12), 4705–4733.

Patricola, C.M., O'Brien, J.P., Risser, M.D., Rhoades, A.M., O'Brien, T.A., Ullrich, P.A., Stone, D.A. & Collins, W.D. (2019). Maximizing ENSO as a source of western US hydroclimate predictability. Clim. Dyn., https://doi.org/10.1007/s00382-019-05004-8.

Penland, C. & Sardeshmukh, P.D. (1995). The Optimal growth of tropical sea surface temperature anomalies. J. Climate, 8, 1999-2024.

Planton, Y., Vialard, J., Guilyardi, E., Lengaigne, M. & Izumo, T. (2018). Western Pacific oceanic heat content: A better predictor of El Niño than La Niña. *Geophys. Res. Lett.*, **45**, 9824-9833.

Poli, P., et al. (2016). ERA-20C: An atmospheric reanalysis of the twentieth century. J. Climate, 29, 4083-4097.

Power, S.B., Casey, T., Folland, C., Colman, A. & Metha, V. (1999). Interdecadal modulation of the impact of ENSO on Australia. Clim. Dyn., 15, 319-324.

Puy, M., Vialard, J., Lengaigne, M., Guilyardi, E., DiNezio, P. N., Voldoire, A., Balmaseda, M., Madec, G., Menkes, C. & McPhaden, M. J. (2019). Influence of westerly wind event stochasticity on El Niño amplitude: The case of 2014 vs. 2015. Clim. Dyn., 52, 7435-7454.

Radenac, M.-H., Léger, F., Singh, A., & Delcroix, T. (2012). Sea Surface Chlorophyll signature in the tropical Pacific during eastern and central Pacific ENSO events. *J. Geophys. Res.*, **117**, C04007, doi:10.1029/2011JC007841.

Rayner, N. A. et al. (2003). Global analyses of sea surface temperature, sea ice, and night marine air temperature since the late nineteenth century. *J. Geophys. Res.,* 108, 4407, https://doi.org/10.1029/ 2002JD002670.

Rohde, R. et al. (2013). A new estimate of the average Earth surface land temperature spanning 1753 to 2011. Geoinf. Geostat. Overview, 1, https://doi.org/10.4172/2327-4581.1000101.

Rodgers, K. B., Friederichs, P., & Latif, M. (2004). Tropical Pacific decadal variability and its relation to decadal modulations of ENSO. *Journal of Climate.* 17(19), 3761–3774.

Rogers, J.C. (1981). The North Pacific Oscillation. J. Climatol., 1, 39-52.

Ropelewski, C.F., & Halpert, M.S. (1987). Global and regional scale precipitation patterns associated with El Niño/Southern Oscillation. *Mon. Wea. Rev.*, **115**, 1606-1626.

Shi, J., Fedorov, A.V., & Hu, S. (2019). North Pacific temperature and precipitation response to El Niño-like equatorial heating: Sensitivity to forcing location. Clim. Dyn.. https://doi.org/10.1007/s00328-019-04655-x.

Smith, R. et al. (2010). The Parallel Ocean Program (POP) reference manual, Ocean component of the Community Climate System Model (CCSM), LANL Tech. Report, LAUR-10-01853, 141 pp.

Sun, T., & Okumura, Y. M. (2020). Impact of ENSO-like tropical Pacific decadal variability on the relative frequency of El Niño and La Niña . *Geophysical Research Letters,* revised.

Takahashi, K., Montecinos, A., Goubanova, K., & Dewitte, B. (2011). ENSO regimes: Reinterpreting the canonical and Modoki El Niño. *Geophys. Res. Lett.*, **38**, L10704, doi:10.1029/2011GL047364.

Thompson, C. J., & Battisti, D. S. (2001). A linear stochastic dynamical model of ENSO. Part II: Analysis. *Journal of Climate.* 14(4), 445–466.

Timmermann, A., et al. (2018). El Niño Southern Oscillation complexity. Nature, 559, 535-545.

Tippett, M.K. & Barnston, A.G. (2008). Skill of multimodel ENSO probability forecasts. Mon. Wea. Rev., 136, 3933-3946.

Trenberth, K. E., & Shea, D. J. (1987). On the evolution of the Southern Oscillation. *Monthly Weather Review.* 115(12), 3078–3096.

Trenberth, K. E., & Hurrell, J. W. (1994). Decadal atmosphere-ocean variations in the Pacific. *Climate Dynamics.* 9(6), 303–319.

Trenberth, K.E., Caron, J.M., Stepaniak, D.P. &Worley, S. (2002). Evolution of El Niño-Southern Oscillation and global atmospheric surface temperatures. J. Geophys. Res., 107, 4065, doi:10.1029/2000JD000298.

Turk, D., Meinen, C.S., Antoine, D., McPhaden,M. J., & Lewis, M.R. (2011). Implications of changing El Niño patterns for biological dynamics in the equatorial Pacific Ocean. *Geophys. Res. Lett.*, **38**, L23603, doi:10.1029/2011GL049674.

Verdon, D. C., & Franks, S. W. (2006). Long-term behaviour of ENSO: Interactions with the PDO over the past 400 years inferred from paleoclimate records. *Geophysical Research Letters.* 33(6), L06712, doi:10.1029/2005GL025052.

Vimont, D. J., Battisti, D. S. & Hirst, A. C. (2001). Footprinting: A seasonal link between the mid-latitudes and tropics. Geophys. Res. Lett., 28, 3923-3926.

Wang, B., & An, S.-I. (2002). A mechanism for decadal changes of ENSO behavior: Roles of background wind changes. *Climate Dynamics.* 18(6), 475–486.

Wittenberg, A. T. (2009). Are historical records sufficient to constrain ENSO simulations? *Geophys. Res. Lett.*, **36**, L12702. doi: 10.1029/2009GL038710

Wittenberg, A. T., Rosati, A., Delworth, T. L., Vecchi, G. A., & Zeng, F. (2014). ENSO modulation: Is it decadally predictable? *J. Climate*, **27**, 2667-2681. doi: 10.1175/JCLI-D-13-00577.1

Wu, X., Okumura, Y. M., & DiNezio, P. N. (2019). What controls the duration of El Niño and La Niña events? *Journal of Climate.* 32(18), 5941–5965.

You, Y. & Furtado, J. C. (2017). The role of South Pacific atmospheric variability in the development of different types of ENSO. Geophys. Res. Lett., 44, 7438-7446.

Zhang, H., Clement, A. & Di Nezio, P. (2014). The South Pacific meridional mode: A mechanism for ENSO-like variability. J. Climate, 27, 769-783.

Zhang, Y., Wallace, J.M., & Battisti, D.S. (1997). ENSO-like interdecadal variability: 1900-93. J. Climate, 10, 1004-1020.